universe

MDPI

Article

Energetic Particles and High-Energy Processes in Cosmological Filaments and Their Astronomical Implications

Kinwah Wu [1,2,*], Ellis R. Owen [3,*], Qin Han [1], Yoshiyuki Inoue [3,4,2] and Lilian Luo [1]

[1] Mullard Space Science Laboratory, University College London, Holmbury St. Mary, Surrey RH5 6NT, UK; qin.han.21@ucl.ac.uk (Q.H.); lilian.luo.22@ucl.ac.uk (L.L.)
[2] Kavli Institute for the Physics and Mathematics of the Universe (WPI), UTIAS, The University of Tokyo, Kashiwa 277-8583, Chiba, Japan
[3] Theoretical Astrophysics, Department of Earth and Space Science, Graduate School of Science, Osaka University, Toyonaka 560-0043, Osaka, Japan; yinoue@astro-osaka.jp
[4] Interdisciplinary Theoretical & Mathematical Science Program (iTHEMS), RIKEN, 2-1 Hirosawa, Wakō 351-0198, Saitama, Japan
* Correspondence: kinwah.wu@ucl.ac.uk (K.W.); erowen@astro-osaka.jp (E.R.O.)

Abstract: Large-scale cosmic filaments connect galaxies, clusters, and voids. They are permeated by magnetic fields with a variety of topologies. Cosmic rays with energies up to 10^{20} eV can be produced in astrophysical environments associated with star-formation and AGN activities. The fate of these cosmic rays in filaments, which cannot be directly observed on Earth, are rarely studied. We investigate the high-energy processes associated with energetic particles (cosmic rays) in filaments, adopting an ecological approach that includes galaxies, clusters/superclusters, and voids as key cosmological structures in the filament ecosystem. We derive the phenomenology for modelling interfaces between filaments and these structures, and investigate how the transfer and fate of energetic cosmic ray protons are affected by the magnetism of the interfaces. We consider different magnetic field configurations in filaments and assess the implications for cosmic ray confinement and survival against hadronic pion-producing and photo-pair interactions. Our analysis shows that the fate of the particles depends on the location of their origin within a filament ecosystem, and that filaments act as 'highways', channelling cosmic rays between galaxies, galaxy clusters, and superclusters. Filaments can also operate as cosmic 'fly paper', capturing cosmic ray protons with energies up to 10^{18} eV from cosmic voids. Our analysis predicts the presence of a population of $\sim 10^{12}$–10^{16} eV cosmic ray protons in filaments and voids accumulated continually over cosmic time. These protons do not suffer significant energy losses through photo-pair or pion production, nor can they be cooled efficiently. Instead, they form a cosmic ray fossil record of the power generation history of the Universe.

Keywords: astroparticle physics; cosmic rays; magnetic fields; cosmological filaments; cosmological voids; (galaxy) clusters; galaxies; hadronic interactions; radiative processes

Citation: Wu, K.; Owen, E.R.; Han, Q.; Inoue, Y.; Luo, L. Energetic Particles and High-Energy Processes in Cosmological Filaments and Their Astronomical Implications. *Universe* **2024**, *10*, 287. https://doi.org/10.3390/universe10070287

Academic Editor: Mark Henriksen

Received: 26 May 2024
Revised: 25 June 2024
Accepted: 27 June 2024
Published: 1 July 2024

1. Introduction

Filaments, walls, and voids are the largest structures in the Universe. Filaments are diffuse media connecting lower-order hierarchical structures, such as the gravitationally bound galaxy clusters and groups. They contain dark matter and baryons (gas), but the baryons contribute only about 5–10% of the filament mass (see, e.g., [1,2]). The baryon density in filaments is about 10–100-times higher than the cosmic average value at redshift $z = 0$ [2–4], which is about 4×10^{-31}g cm^{-3} [5]. This gas is considered as a candidate for a major invisible 'missing' constituent of baryons in the Universe (cf. the 'missing baryon problem'; Ref. [6]). Baryons in filaments mostly consist of hot ionised gas and warm partially ionised gas. This multi-phase mixture is often referred to as the warm–hot intergalactic medium (WHIM). The current view is that the WHIM is heated by shocks

generated by energetic events associated with structure formation, together with feedback processes from galaxies, e.g., galaxy mergers, galactic outflows, or active galactic nucleus (AGN) activities (see [7–9]).

The Universe is permeated by magnetic fields, and naturally, filaments are magnetised. The strengths of their magnetic fields inferred from recent observations are ∼10–60 nG [2,10,11], but their origin is yet to be resolved. While they could be partly cosmological in nature (see [11]), star-forming activities in galaxies may play a non-negligible role in magnetising filaments [12–14], especially in regions where the filaments meet the circumgalactic medium (CGM) (see [15]).

Stacking observations in X-rays and radio wavebands (see [2,16]) indicate the presence of highly energetic particles, often referred to as cosmic rays, in filaments. (Here and hereafter, unless otherwise stated, we adopt the terminology energetic particles and cosmic rays interchangeably.) There is no direct observational evidence that the cosmic rays and magnetic fields in filaments are in energy equipartition. The cosmic ray particles may be accelerated in situ in the filaments, e.g., through accretion shocks near structures [17], or they may be produced elsewhere, e.g., in star-forming galaxies (see, e.g., [18]), or in AGNs and their jets (see, e.g., [19]), then transported into the filaments. The structure and thermodynamics of filaments evolve as a consequence of cosmological structural formation dynamics (see [20]). Star-forming and AGN activities are also not uniform across cosmic history. Hence, the properties and composition of energetic particles in filaments evolve over time.

In this work, we investigate the high-energy processes associated with energetic particles (cosmic rays) in cosmological filaments, and determine their consequences. We organise the paper as follows. In Section 2, we describe hadronic processes in astrophysical environments; in Section 3, we elaborate how energetic particles are magnetically confined in various configurations of filament magnetic fields; in Section 4, we illustrate how particles are transferred between filaments and voids, superclusters/clusters, and galaxies by following the cosmic journey of individual particles. In Section 5, we discuss the implications for the presence of populations of energetic particles in cosmic filaments resulting from the interactions and transfer processes in filament ecosystems. A short conclusion is presented in Section 6.

2. Hadronic Interactions in Astrophysical Environments

Cosmic rays are a mix of particles of different species. At energies below 10^{19} eV, hadronic cosmic rays in galactic and extragalactic environments are believed to be mostly protons (H nuclei). Heavier nuclei dominate at higher energies. This seems to be supported by the observed composition of cosmic rays arriving on Earth (see, e.g., analysis of data obtained by the Pierre Auger Observatory [21]). The dominance of heavy nuclei at energies above 10^{19} eV implies that the transport of multi-species cosmic rays and the acceleration of heavy nuclei are more complicated than scenarios of cosmic ray attenuation based solely on the Greisen–Zatsepin–Kuzmin (GZK) effect [22,23]. Adding to this complexity, the composition of cosmic rays and their properties are not uniform in space or over cosmological time. It is a challenging task to disentangle these factors and the effects they induce, given that our understanding of structural formation at the sub-cluster and galactic levels is still incomplete and our capability to confidently identify and model cosmic particle accelerators beyond the framework of stochastic processes in shocks is limited. Even on the scale of the Solar System, we cannot rely on information about the composition of cosmic rays arriving on Earth to infer the energy distribution and composition of cosmic rays in local interplanetary space. For example, cosmic ray baryons observed on Earth at sea level are, in fact, mostly neutrons [24,25]. Some in situ measurements by spacecraft have extended the domain of our direct measurements of cosmic rays [26], extending to the edge of the Solar System [27,28] and local interstellar space beyond the heliosphere [29]. However, beyond the Solar System and immediate local region of interstellar space, our knowledge of cosmic rays can only be inferred from simulations (see

[30,31]), or phenomenological modelling (e.g., [32–35]), often based on information derived from observations in γ-rays (e.g., [36–38]), radio (e.g., [39,40]), or at other wavelengths (e.g., [41–44]). To date, volumes of manuscripts have been published in efforts devoted towards understanding cosmic ray composition and their properties in galaxies and in intergalactic media (IGM). Despite this, it remains a subject of ongoing discussion and debate (for recent reviews, see [45–48]).

Cosmic rays interact with radiation and baryons in interstellar and intergalactic space; hence, their content and composition evolve as they propagate. Without loss of generality, we illustrate the interactions with a proton (or a neutron) interacting with a photon or with another proton. These processes are referred to as pγ (or nγ for neutron) and pp interactions, respectively. The pγ interaction is dominated by two channels. The first is photo-pion production. This, including the subsequent interactions and its decay branching, proceeds as follows (resonant states not shown) (see, e.g., [49]):

$$\mathrm{p} + \gamma \longrightarrow \begin{cases} \mathrm{p}\pi^0 \longrightarrow \mathrm{p}\, 2\gamma \\ \mathrm{n}\pi^+ \longrightarrow \mathrm{n}\,\mu^+\nu_\mu \\ \qquad\qquad \hookrightarrow \mathrm{e}^+\nu_\mathrm{e}\bar{\nu}_\mu \end{cases} ; \tag{1}$$

$$\mathrm{n} + \gamma \longrightarrow \begin{cases} \mathrm{p}\,\pi^- \longrightarrow \mathrm{p}\,\mu^-\bar{\nu}_\mu \\ \qquad\qquad \hookrightarrow \mathrm{e}^-\bar{\nu}_\mathrm{e}\nu_\mu \\ \mathrm{n}\,\pi^0 \longrightarrow \mathrm{n}\, 2\gamma \end{cases} . \tag{2}$$

The minimum energy for a proton, $E_\mathrm{p}\,(=\gamma m_\mathrm{p}[c]^2)$, to initiate a chain of pion production in a radiation field is given by

$$\gamma_\mathrm{p} = \frac{1}{4}\frac{m_\mathrm{p}[c]^2}{\epsilon_\mathrm{ph}}\left[\left(\frac{m_\mathrm{n}}{m_\mathrm{p}} + \frac{m_{\pi^+}}{m_\mathrm{p}}\right)^2 - 1\right] \approx \frac{2}{25}\frac{m_\mathrm{p}[c]^2}{\epsilon_\mathrm{ph}} \tag{3}$$

(for $m_\mathrm{p}[c]^2 \gg \epsilon_\mathrm{ph}$) where c is the speed of light, γ_p is the Lorentz factor of the proton, ϵ_ph is the energy of the photon, and m_p, m_n, and m_{π^+} are the masses of the proton, neutron, and charged pion, respectively.

The second channel of the pγ interaction is Bethe–Heitler photo-pair production [50]. This proceeds as follows:

$$\mathrm{p}' + \gamma \rightarrow \mathrm{p} + l^+ + l^- , \tag{4}$$

where p$'$ and p are the cosmic ray protons before and after the pair-production process, respectively. $l^\pm$ are the produced lepton–anti-lepton pair, which are dominated by electrons and positrons [51,52], although heavier leptons can also be formed [53].

The major channels for the pp interaction and their branching are as follows:

$$\mathrm{p} + \mathrm{p} \longrightarrow \begin{cases} (\mathrm{p}\Delta^+) \longrightarrow \begin{cases} \mathrm{p\,p}\,\pi^0\,\xi_0(\pi^0)\,\xi_\pm(\pi^+\pi^-) \\ \mathrm{p\,p}\,\pi^+\pi^-\,\xi_0(\pi^0)\,\xi_\pm(\pi^+\pi^-) \\ \mathrm{p\,n}\,\pi^+\,\xi_0(\pi^0)\,\xi_\pm(\pi^+\pi^-) \end{cases} \\ (\mathrm{n}\Delta^{++}) \longrightarrow \begin{cases} \mathrm{n\,p}\,\pi^+\,\xi_0(\pi^0)\,\xi_\pm(\pi^+\pi^-) \\ \mathrm{n\,n}\,\pi^+\pi^+\xi_0(\pi^0)\,\xi_\pm(\pi^+\pi^-) \end{cases} \end{cases} . \tag{5}$$

Unlike the pγ interaction, the dominant channels of the pp interaction tend to produce resonance particles (e.g., [54–56]), such as Δ^+ and Δ^{++}. Their subsequent decays give rise to multiple pions. Among these, neutral pions produce γ-rays, while charged pions produce leptons and their corresponding neutrinos. In pp interactions, decays of the Δ resonances restore the number of strange-zero ($S = 0$) baryons of the $S = 1/2$ ground-state

baryon octet while producing the lowest mass strange-zero pseudo-scalar mesons of the spin-zero nonet.

In the centre-of-momentum frame, the threshold energy of the protons, $\tilde{\gamma}_{\rm p} m_{\rm p}[c]^2$, for pion production in a pp interaction is the available energy of the protons in a collision, which excites a $\mathrm{p}\Delta^+$ or an $\mathrm{n}\Delta^{++}$ intermediate state:

$$\begin{cases} 2\,\tilde{\gamma}_{\rm p} m_{\rm p} \approx m_{\rm p} + m_{\Delta^+} \\ 2\,\tilde{\gamma}_{\rm p} m_{\rm n} \approx m_{\rm p} + m_{\Delta^{++}} \end{cases} , \tag{6}$$

which gives

$$\tilde{\gamma}_{\rm p} \approx \frac{1}{2}\left[\frac{m_{\rm x}}{m_{\rm p}} + \frac{m_\Delta}{m_{\rm p}}\right] , \tag{7}$$

where $\mathrm{x} \in \{\mathrm{p}, \mathrm{n}\}$ and m_Δ is the mass of the Δ resonance particle, which is about $1.232\,\mathrm{GeV}/[c]^2$. The pions resulting from the decay of the Δ particles, therefore, cannot be at rest in the centre-of-momentum frame, but instead have a substantial amount of kinetic energy. Moreover, there would be a dichotomy in the energy distribution of the pions. Thus, the pions retain certain information about the energetic protons that initiate a pp interaction.

The proton threshold energy for pion production in a pp interaction is only slightly above $m_{\rm p}[c]^2$, and is insensitive to parameters other than the rest masses of the particles involved. The situation is very different in the pγ interaction, where the threshold energy of the protons is dependent on the photon energy in the radiation field. The wavelength of the cosmic microwave background (CMB) radiation in the current epoch (redshift $z = 0$) is about 2 mm. The CMB spectrum has a peak photon energy of $\epsilon_{\rm ph} \approx 6.63 \times 10^{-4}$ eV. The proton threshold energy is, therefore, $E_{\rm p} \approx 10^{20}$ eV (for $\gamma_{\rm p} > 1.1 \times 10^{11}$). Starburst galaxies tend to have a prominent infra-red (IR) emission component, peaking at wavelengths of ∼50–100 μm (e.g., M82; see [57,58]). The photon energy at 75 μm is $\epsilon_{\rm ph} \approx 1.65 \times 10^{-2}$ eV, giving a proton threshold energy of $E_{\rm p} \approx 4.3 \times 10^{18}$ eV (for $\gamma_{\rm p} > 4.6 \times 10^{9}$). The spectrum of a disk or elliptical galaxy generally peaks at wavelengths around 1.0 μm (e.g., M101 and NGC 5018; see [57]), and a substantial fraction of the photons in the radiation field would have energies of $\epsilon_{\rm ph} \approx 1.25$ eV, which implies a characteristic proton threshold energy of $E_{\rm p} \approx 5.6 \times 10^{16}$ eV (for $\gamma_{\rm p} > 6.0 \times 10^{7}$).

3. Confinement and Trapping of Energetic Particles

3.1. Filaments as Mass Condensates and Particle Interactions

Because of the lack of direct observations, our current knowledge of large-scale cosmic filaments is primitive. Not much is known about their geometrical properties (such as their thickness), their dark matter distribution, the thermodynamic properties of filament gas, the configurations and origin(s) of filament magnetic fields, or their evolution over cosmological time. Our understanding of cosmic filaments is derived mostly from numerical simulations (see [59–62]). Despite this, there is no doubt that filaments are very important components in the hierarchy of cosmological structures. Indeed, most of the mass in the Universe is confined in filaments in the current epoch, slightly exceeding the total mass contained in galaxy clusters [59].

Clusters are young objects. While proto-clusters with redshifts as high as $z \sim$ (6–7) are present [63] and some clusters with a developed thermalised intra-cluster medium (ICM) could have formed slightly above $z \sim 2$ (see [64]), the majority of fully-fledged clusters are found to reside at $z < 1$ (see [65]). Filamentary structures, in contrast, appear well before $z \sim 4$ (see [61]), implying these have always been the dominant mass condensates of the Universe. Embedded in high-z filaments are galaxies and groups of galaxies in the early stages of their lives. Stars are formed in these galaxies, and supermassive black holes grow through merging and accretion. These black holes would appear as AGNs when they

accrete gas from their surroundings. This has very significant implications from the perspective of multi-messenger astronomy involving highly energetic non-photonic particles.

It is generally accepted that starburst galaxies and AGNs are capable of producing energetic particles of energies from a GeV to above a PeV [45,66–68]. Cosmic star-formation activities peak at $z \sim 2$ [69] (often referred to as the 'cosmic noon' (see [70] for a review)). AGN activities also peak at $z \sim 2$ [71]. This implies that most of the energetic particles produced in the Universe must pass through filaments before they can escape to the cosmic voids, or are somehow trapped in filaments after they have left their galaxy of origin. Hadronic particles in cosmic voids, if they have sufficient energies, interact with CMB photons to produce lower energy hadronic particles and leptons. They also lose some fraction of their energy through an adiabatic process due to cosmological expansion.

Like clusters and galaxies, filaments evolve. Simulations show that they stretch and thicken over time (see, e.g., [59–61]). The density and thermal conditions of the gas and particles in filaments, therefore, do not stay constant. Filaments are, in fact, large-scale ecosystems. They exchange energy and chemicals with the galaxies embedded within them, and the clusters hooked onto them through processes such as accretion and outflows (see, e.g., [72]). In addition, filaments are also irradiated by the stars in galaxies and by AGNs, which could be a heating source that can modify their thermal conditions.

The evolution of the thermal and mechanical properties of filaments, together with the development of filament magnetic fields, determines whether energetic particles (including nuclei, baryons, and leptons) produced by star-formation or AGN activities can break the confinement of their host galaxies. Generally, energetic heavy nuclei will degrade into lighter nuclei or single baryons through spallation collisions or hadronic interactions. Cosmic ray baryons will interact with photons in the radiation field or with other baryons, resulting in lepton pair and pion production (see Section 2). Charged pions then decay to produce leptons and neutrinos, while neutral pions decay to form γ-ray photons. Heavier leptons will decay into lighter leptons and their corresponding neutrinos, eventually to electrons/positrons and electron neutrinos. Energetic electrons and positrons gradually lose their energy through radiative processes.

An important factor that determines whether energetic particles in filaments undergo pp and pγ interactions is the size of filaments. Maps of large-scale structures in the Universe have shown that filaments have lengths of several tens of Mpc [73,74], with the longest ones exceeding 100 Mpc [75]. The thickness of filaments is not easily determined directly from observations; however, simulations have indicated that the thickness of filament spines are $\sim$2 Mpc (see, e.g., [59,60,76]), and filaments in the current epoch ($z = 0$) could have a thickness of $\sim$4 Mpc [61].

Figure 1 shows the interaction lengths of pp and pγ interactions in cosmological filaments and voids at redshifts $z = 0$, 2, and 7 (respectively, corresponding to the current epoch, the cosmic noon when star-formation and AGN activities peaked, and the cosmic dawn during the process of cosmological reionisation). The parameters adopted for the calculations are summarised in Appendix A. Given that the width of filaments would not exceed 4 Mpc at any epoch, pp or pp-like interactions are inconsequential for unconfined energetic baryons, which are unaffected in filaments and voids. At the current epoch ($z = 0$), unconfined protons are not attenuated by pγ interactions in filaments; only protons with energies above $\sim 3 \times 10^{20}$ eV would be degraded by interactions with CMB photons (cf. the GZK effect [77,78]). At cosmic noon ($z = 2$), unconfined protons of energies below 10^{19} eV would not be affected when traversing a filament, but protons with energies above 10^{17} eV could undergo pγ interactions when they travel along a filament or cross a void. At cosmic dawn ($z = 7$), unconfined protons of energies above 10^{17} eV would be attenuated by pγ interactions in both filaments and voids.

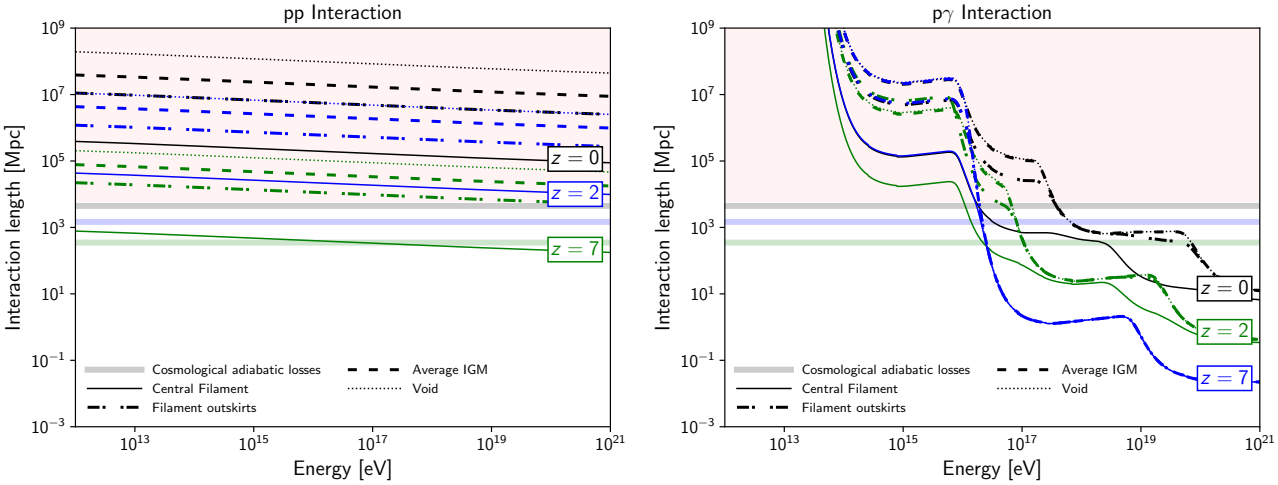

Figure 1. The interaction lengths of protons undergoing pp interaction processes (**left** panel) and pγ processes (**right** panel) for photo-pair and photo-pion production in cosmic filaments and voids, at redshifts of $z = 0$, 2, and 7. The calculations are based on those for the hadronic pp and pγ interactions in Ref. [79]. The parameters adopted for the calculations are shown in Appendix A. The length scales for proton adiabatic losses at $z = 0$, 2, and 7 due to cosmological expansion are also shown for comparison. These assume a ΛCDM cosmology with cosmological parameters of $H_0 = 67.4$ km s^{-1} Mpc^{-1}, $\Omega_{\rm m} = 0.315$, and $\Omega_\Lambda = 0.685$ and negligible curvature and radiation energy densities (following the 2018 *Planck* results; Ref. [80]). The distance to the event horizon of the Universe at the current epoch is roughly the same as the adiabatic loss length scale of protons at $z = 0$. Interaction lengths above this scale (indicated by the pink shaded regions in the panels) are not of astrophysical consequence, but are shown for completeness.

The Universe has a finite age, and the cosmic horizon has a finite extent. Without deflections, energetic protons could propagate over distances of a few Gpc. From this, together with the interaction length comparisons shown in Figure 1, we come to the following conclusions: (i) cosmic ray protons with energies below about 10^{16} eV will not be attenuated in filaments or voids; (ii) energetic protons do not directly deposit energy into filament gas; (iii) energetic protons below 10^{16} eV retain a substantial amount of their energy when they are confined in filaments, until they collide with other baryons or high-energy photons (such as the keV X-rays from AGNs).

3.2. Gyration of Charged Particles

The radius of gyration, the Larmor radius $r_{\rm L}$, of a particle with a charge Ze and a mass m around a magnetic field $\boldsymbol{B}$ is given by

$$r_{\rm L} = \gamma\beta \sin\theta \, \frac{mc^2}{|Ze\boldsymbol{B}|} = 1.7 \times 10^{12} \, \gamma\beta \left(\frac{\sin\theta}{Z}\right) \left(\frac{m}{m_{\rm e}}\right) \left(\frac{|\boldsymbol{B}|}{\rm nG}\right)^{-1} {\rm cm} \, . \tag{8}$$

Here, $\gamma (= (1-\beta^2)^{-1/2})$ is the Lorentz factor of the particle, $\boldsymbol{\beta}$ the velocity of the particle (normalised to the speed of light c), and $\theta (= \cos^{-1}(\boldsymbol{\beta} \cdot \boldsymbol{B}/|\boldsymbol{B}|))$ is its pitch angle. We may define a parameter:

$$\zeta_{\rm L} \equiv \frac{1}{2\pi\mathcal{D}} \int_{2\pi} {\rm d}\Omega \; r_{\rm L} \, , \tag{9}$$

where $\mathcal{D}$ is the characteristic size of a domain in which the threading magnetic field has a coherent structure. For a relativistic nucleus ($\beta \to 1$, $\gamma \gg 1$) of mass number A,

$$\zeta_{\rm L,nu} \approx 8.5 \times 10^{-8} \left(\frac{A}{Z}\right) \left(\frac{E_{\rm nu}}{1\,{\rm TeV}}\right) \left(\frac{\mathcal{D}}{1\,{\rm Mpc}}\right)^{-1} \left(\frac{\mathcal{B}}{10\,{\rm nG}}\right)^{-1} , \tag{10}$$

where $E_{\rm nu}$ is the energy of the nucleus. The parameter $\zeta_{\rm L,nu}$ is a measure of whether or not a charged nucleon would be confined in a domain of extent $\mathcal{D}$ with a coherent magnetic structure of a characteristic field strength $\mathcal{B}$. This variable $\zeta_{\rm L,nu}$ has no explicit dependence on the mass of the charged particle, but instead depends on the ratio (A/Z). The parameter $\zeta_{\rm L,nu}$ not only determines if a nucleon of A/Z can be confined, but also sets a criterion for the maximum energy a nucleon can acquire through stochastic acceleration in a region involving magnetic confinement in the acceleration process (cf. the Hillas criterion [81]). A direct scaling of the expression in Equation (10) gives a corresponding expression for a relativistic electron/positron of energy $E_{\rm e}$:

$$\zeta_{\rm L,e} \approx 8.5 \times 10^{-11} \left(\frac{E_{\rm e}}{1\,{\rm GeV}}\right)\left(\frac{\mathcal{D}}{1\,{\rm Mpc}}\right)^{-1}\left(\frac{\mathcal{B}}{10\,{\rm nG}}\right)^{-1}. \tag{11}$$

Protons with $\zeta_{\rm L,p}\ (= \zeta_{\rm L,nu}|_{(A/Z)=1}) > 1$ and electrons/positrons with $\zeta_{\rm L,e} > 1$ are able to break magnetic confinement. In most astrophysical situations, the energies of electrons would not greatly exceed PeV levels. Thus, $\zeta_{\rm L,e} \ll 1$ would be expected in filament environments.

3.3. Magnetic Field Configurations

While there is a consensus that cosmic filaments are magnetised, little is known about the properties of their magnetic fields, including their strength, their global and local topology, and their connectedness to the internal magnetic fields of lower hierarchical systems linked to the filaments (e.g., groups or clusters) or embedded within them (e.g., field galaxies). Direct measurements of magnetic fields beyond galaxy cluster scales is a great technical challenge. Currently, only loose constraints can be derived for the strengths of the magnetic fields in filaments or in voids, and we practically have no reliable information about the field topology or how magnetic fields in filaments and voids interface. The strengths of magnetic fields in voids are inferred to be below nG, based on the directional anisotropy observed in ultra-high-energy (UHE) cosmic rays [82], the absence of a trend in the rotation measure (RM) of distant radio sources over redshift [83], and the lack of any clear detection of pair echoes or halos from distant γ-ray point sources due to deflected electromagnetic cascades (e.g., [84,85]). Magnetic fields in filaments are estimated to be around 30 nG [2,11]. While we may derive such constraints on their strengths based on arguments invoking thermodynamics (e.g., energy equipartition between particles and the magnetic field) or radiative processes (such as synchrotron emission and/or Compton scattering), we still do not have a reliable means to determine the configurations of magnetic fields in filaments theoretically or observationally.

The confinement and transport of energetic particles in filaments is sensitively dependent on the topological properties and effective strengths of the magnetic fields. Modelling how energetic charged particles behave in cosmological filament environments is not a trivial generalisation of modelling how energetic charged particles behave in diffuse media on stellar and galactic scales. This is partly due to the sheer scale of cosmological filaments, but also because the fate of energetic particles is dependent on the properties of filaments at different stages of their cosmological evolution. It is also partly due to the connectedness of the filament magnetic field to the magnetic fields of the embedded galaxies (where energetic charged particles originate) and the clusters/superclusters where the filaments terminate. Filaments can, therefore, be considered as a part of a larger ecological web, in which particles are energised, destroyed, converted, and recycled.

We now lay out a conceptual framework, which provides a basis for meaningful discussion of the fate of energetic particles in their complex interplay with filament environments. Magnetic fields undoubtedly regulate the destruction, conversion, and recycling of energetic particles in cosmological filaments. Self-gravitating astrophysical systems generally have round shapes if they are gravitationally supported (e.g., stars, elliptical galaxies, and galaxy clusters) or disk shapes if they are supported by angular momentum (e.g., proto-stellar systems and disk galaxies). Filaments are the only self-gravitating sys-

tems that can persist over long timescales (cf. Hubble time), with elongated structures. The unique geometry of filaments allows them to harbour a coherent magnetic structure along their symmetry axis over length scales substantially larger than their thickness.

With this in mind, we may consider a filament segment of characteristic linear size ℓ within a filament of length $\mathcal{L}$, where $\mathcal{L} \gg \ell$. This segment is part of a long filament section, which is permeated by a magnetic field. The magnetic field can be decomposed into a relatively well-ordered large-scale component $\boldsymbol{B}_{\rm g}$ and a disordered smaller scale component $\boldsymbol{B}_{\rm s}$, i.e.,

$$\boldsymbol{B} = \boldsymbol{B}_{\rm g} + \boldsymbol{B}_{\rm s} \,. \tag{12}$$

The large-scale component serves as the field substratum. It can be further decomposed into two orthogonal components: $\boldsymbol{B}_{\rm g} = \boldsymbol{B}_{\parallel} + \boldsymbol{B}_{\phi}$, where $\boldsymbol{B}_{\phi}$ is the global toroidal component, presumably supported by a large-scale current flow along the filament, and $\boldsymbol{B}_{\parallel}$ is the parallel component contributing to the global directional magnetic flux aligned with the orientation of the filament. In the absence of a large-scale current, $\boldsymbol{B}_{\rm g} = \boldsymbol{B}_{\parallel}$. Without losing generality, we simply assume that the large-scale current is negligible, i.e., $|\boldsymbol{B}_{\parallel}| \gg |\boldsymbol{B}_{\phi}|$. The smaller scale disordered field component, $\boldsymbol{B}_{\rm s}$, contributes to the rest of the total magnetic field in the filament segment. We assume that the small-scale field component is statistically isotropic (i.e., it has no preferential orientation), and statistically homogeneous (i.e., it is invariant under spatial translation). As the magnetic field is divergence-free, the magnetic fluxes of the small-scale disordered field component passing through an arbitrary surface constructed within the filament, with an area similar to or larger than the cross-section of a galaxy, is statistically zero. These properties of an arbitrary surface do not hold for the large-scale field component, though its magnetic flux entering and leaving a volume element within the filament segment is strictly zero. We shall demonstrate in later sections that such differences between the large-scale and the small-scale field components would have subtle effects on the properties and fate of baryonic cosmic rays in the filaments.

Figure 2 shows six examples of generic field configurations in a filament segment. These configurations are reasonable representations in regions without sizeable substructures such as galaxies, groups, or clusters. They are constructed based on the relative strengths of $\boldsymbol{B}_{\rm g}$ and $\boldsymbol{B}_{\rm s}$, with additional considerations such as large-scale fields along the filament linking a pair of galaxy clusters close by.

In observational and simulation studies, the properties of magnetic fields are often quantified with a coherence length $\lambda_{\rm B}$ (see, e.g., [86,87]). For the convention of magnetic field decomposition that we have adopted, $\boldsymbol{B}_{\rm g}$ would have a larger value for $\lambda_{\rm B}$, while $\boldsymbol{B}_{\rm s}$ would have a smaller value. Note that $\boldsymbol{B}_{\rm g}$ in the field configuration shown in panels 1, 2, and 3 all have $\lambda_{\rm B} \approx \mathcal{D}$, yet the variations in their structures would lead to very different effects on the fate of charged particles. Thus, in a more thorough formulation, a comprehensive description beyond coherence length parameters $\lambda_{\rm B}$ would be necessary, though our approach is still important to provide useful insights into the properties of magnetic fields in the interstellar medium (ISM) or the IGM. For clarity in the field topological analysis, hereafter, we do not consider the coherence length parameter explicitly unless otherwise stated. We instead describe the magnetic fields directly using a two-component $\boldsymbol{B}_{\rm g} - \boldsymbol{B}_{\rm s}$ decomposition.

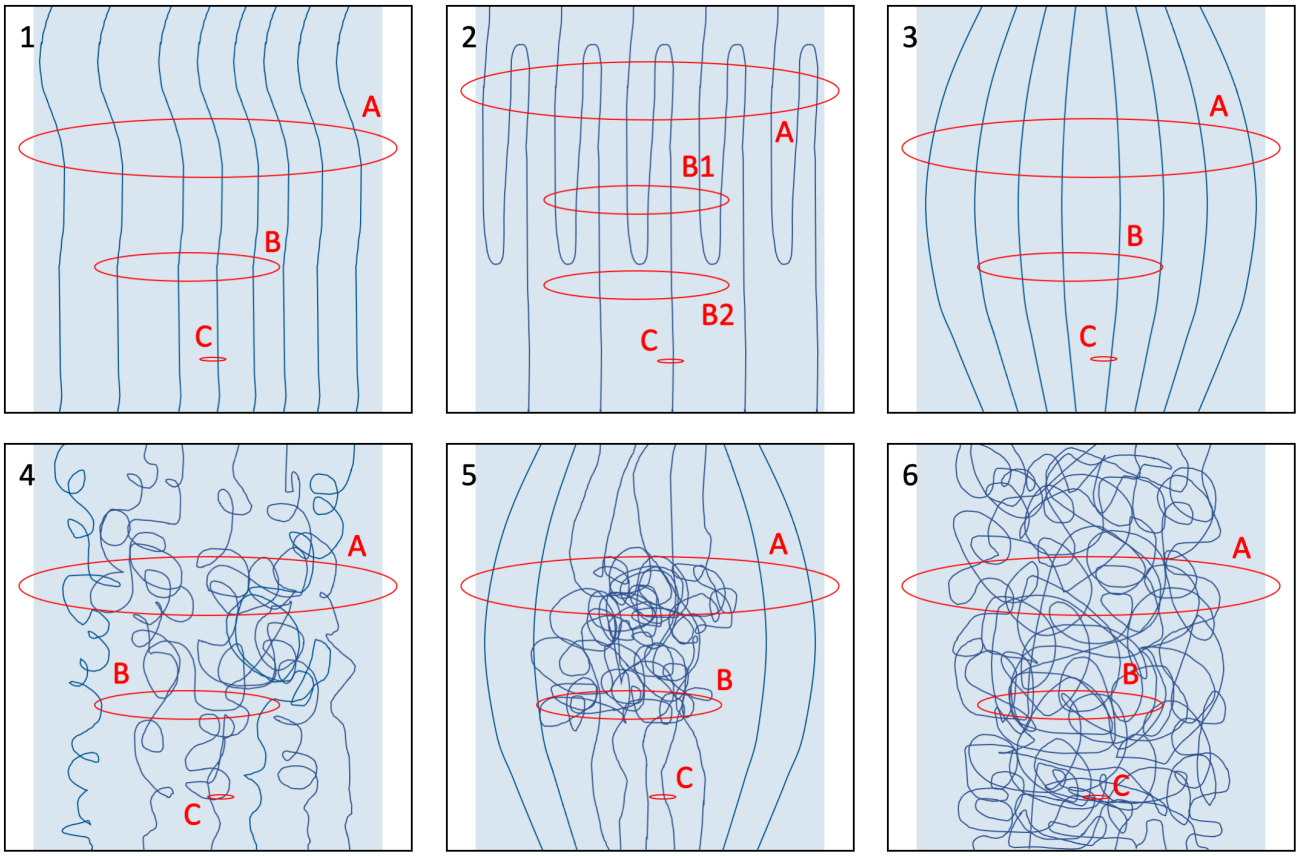

Figure 2. Schematic illustrations of various generic situations for the confinement and transport of energetic charged particles in segments of cosmological filaments (denoted by the shaded light blue region in each panel) threaded by magnetic fields (represented by curved dark blue lines). The gyration of the charged particles in the magnetic fields may be classified into three regimes represented by the red ellipses (gyration orbits), not to scale, marked with A, B (or B1 and B2), and C. The regimes are defined according to the value of $\zeta_{\mathrm{L,p}}$, by setting in Equation (10) (for $A/Z = 1$) the domain extent $\mathcal{D}$ as the width of the filament and characteristic magnetic field strength $\mathcal{B}$ as that given by Equation (13). The orbit types labelled as A correspond to cases where $\zeta_{\mathrm{L,p}} > 1$; the orbit types labelled as B (and B1/B2) correspond to cases where $\zeta_{\mathrm{L,p}} \lesssim 1$; the orbit types labelled as C correspond to cases where $\zeta_{\mathrm{L,p}} \ll 1$. The magnetic fields in the panels have two components, a component with a relatively well-ordered large-scale field configuration within the region (i.e., the presence of a guided field) and a component with disordered smaller scale field configuration. Panel 1 shows a filament segment where the magnetic field is dominated by an ordered large-scale field without orientation reversal. Panel 2 shows a filament segment where the magnetic field is dominated by an ordered large-scale field, but there are field reversals warping parts of the segment. Panel 3 shows a filament segment where the dominant component of the magnetic fields have a bottle configuration. Panel 4 shows a filament segment where the disordered small-scale field components are as prominent as the the large-scale well-ordered component, which has an orientation parallel to the filament. Panel 5 shows a filament segment where a prominent disordered small-scale field component is embedded inside a large-scale component with a bottle configuration. Panel 6 shows a filament segment where the well-ordered large-scale field component is absent, leaving only the presence of a disordered small-scale field component. Note that type B orbits are split into two subgroups, B1 and B2, in panel 2, with the former in the folded field region and the latter outside the folded field region.

In the first three cases shown in Figure 2, the small-scale disordered field component is negligible compared with the large-scale field component. When $|\boldsymbol{B}_{\mathrm{g}}| \gg |\boldsymbol{B}_{\mathrm{s}}|$, the magnetic field is relatively ordered and aligned with the filament orientation (see panel 1). If there is a strong flow along the filaments (e.g., in channelled accretion), Rayleigh–Taylor instabilities

could develop, which may lead to a field folding in some regions in the filament segment (see panel 2). A magnetic bottle field configuration could develop in the region between two embedded galaxies in a filament (see panel 3). This requires that the flow within the filament be dominated by bulk motion instead of turbulent motion. This can occur naturally, and can be understood as follows. The turbulent speeds $v_{\rm turb}$ in the IGM are in the range of 10–50 km s^{-1}, as inferred from observations (e.g., [88,89]). It is generally considered that filaments contain a substantial amount of the WHIM, which has a temperature of $\sim 10^5$–10^7 K. If we take a gas temperature $T \sim 10^6$ K, it gives a sound speed $c_{\rm s} \sim 70\,{\rm km\,s^{-1}}$. Thus, the IGM turbulence is generally subsonic. The flows in filaments are not pressure supported, and it has been argued that shocks are present in filaments [17]. This implies that the bulk flow speed $v_{\rm bulk}$ along the filament is supersonic, i.e., $v_{\rm bulk} > c_{\rm s} > v_{\rm turb}$ (at least in certain regions within a filament).

In the last three cases shown in Figure 2, the small-scale disordered field component is non-negligible compared with the large-scale field component, at least in some regions, or even dominates over the large-scale field component. When the two field components are comparable, the magnetic field in the filament segment would share the characteristics of the two components (see panel 4). While the field lines appear to be entangled, they do not mask the global orientation of the directed large-scale field component. There are also situations where disordered magnetic fields are generated inside a magnetic bottle field configuration (see panel 5) by the turbulence motion of the ionised gas (plasma), or energetic particles trapped inside, or by the presence of a shock caused by colliding outflows from two galaxies. If the filament segment does not have strong bulk flow, it is possible that the disordered field component dominates (see panel 6), reflecting the turbulent nature of the gas in the region.

3.4. Particle Confinement

To determine $\zeta_{\rm L,nu}$ and $\zeta_{\rm L,e}$ for nucleons or electrons of given energies, we need to assign values for $\mathcal{D}$ and $\mathcal{B}$ in Equations (10) and (11). For the value of $\mathcal{D}$, the filament thickness can be adopted as inferred from observations, such as stacking. The value for $\mathcal{B}$ is currently not measurable directly from observations. Instead, it can be derived under certain assumptions, such as the energy equipartition between the magnetic field and non-thermal particles, if the energy content of the emitting particles can be determined from observations. Different field configurations could give the same $\mathcal{B}$. Figure 2 shows examples of magnetic field configurations, with different combinations of $\boldsymbol{B}_{\rm g}$ and $\boldsymbol{B}_{\rm s}$, in a two-component representation. For uncorrelated $\boldsymbol{B}_{\rm g}$ and $\boldsymbol{B}_{\rm s}$, the characteristic field strength is then

$$\begin{aligned}\mathcal{B} &= \sqrt{\langle \boldsymbol{B}_{\rm g}{}^{*} \cdot \boldsymbol{B}_{\rm g}\rangle + \langle \boldsymbol{B}_{\rm s}{}^{*} \cdot \boldsymbol{B}_{\rm s}\rangle + 2\langle \boldsymbol{B}_{\rm g}{}^{*} \cdot \boldsymbol{B}_{\rm s}\rangle} \\ &\approx \sqrt{|\boldsymbol{B}_{\rm g}|^2 + |\boldsymbol{B}_{\rm s}|^2}\,. \end{aligned} \tag{13}$$

For protons in a filament segment with $\{\mathcal{D}, \mathcal{B}\}$, $\zeta_{\rm p}\,(= \zeta_{\rm L,nu}|_{(A/Z=1)})$ will depend only on $E_{\rm p}$, the proton energy. If we set $\mathcal{B} \sim 30\,{\rm nG}$ (a value similar to the field estimated for large-scale filament (see [90])), protons with energies of 3.5×10^{19} eV, 1.1×10^{18} eV, and 3.5×10^{16} eV would have gyration radii of 1 Mpc, 40 kpc, and 1 kpc, respectively. The protons may, therefore, be sorted into three groups, (i) $\zeta_{\rm L,p} > 1$, (ii) $\zeta_{\rm L,p} \lesssim 1$, i.e., slightly smaller than, but of the same order as 1, and (iii) $\zeta_{\rm L,p} \ll 1$, according to their energies. The protons in these groups have their gyration radii larger than, comparable with, but slightly smaller, and much smaller than the thickness of the associated filament, respectively.

We now illustrate how differently the protons in the three groups would behave for different magnetic field configurations (even though they may share the same value for $\mathcal{B}$). We ignore the drift of the protons along the filament for the time being and focus on their motion perpendicular to the filament orientation. Schematic illustrations of the gyration orbits, labelled as A, B (B1/B2), and C for the proton groups (i), (ii), and (iii), respectively, are shown in Figure 2.

As gyration orbit type A exceeds the filament thickness, the protons with this orbit will not be confined to the filament in all cases shown in Figure 2. Gyration orbit type B is slightly smaller than the filament thickness, and proton confinement would occur in this case, at least in principle. However, non-uniformity in the magnetic field will cause these protons to drift across filament. Protons of gyration orbit type B can, therefore, only be confined and survive in the filament over a timescale that depends on the competition between particle interactions and particle escape through cross-field particle diffusion (see, e.g., [91]). Protons of gyration orbit type C will be trapped in the filaments.

The filament segment shown in panel 1 is the generic situation. The lack of $\boldsymbol{B}_{\rm s}$ in this case implies weaker diffusion for protons with gyration orbit type B, compared to the other field configurations in Figure 2. The well-ordered $\boldsymbol{B}_{\rm g}$ aligned along the filament segment also implies that protons with gyration orbit type C could be channelled out from the segment through drift along the field direction.

The filament segment in panel 2 has a field folding region. The magnetic field reversal alters the confinement ability of the region and, hence, that of the filament segment. Protons that should otherwise have been retained according to their energies $E_{\rm p}$ and the characteristic field strength $\mathcal{B}$ in the filament segment (such as those with gyration orbit type B2), can now break free of confinement. Field folding, therefore, opens up a back-door for protons (those with gyration orbit type B1) to leave a filament through direct escape or by fast tracking cross-field diffusion.

Magnetic mirroring in panel 3 will restrict the drift of the protons with gyration orbits smaller than the thickness of the filament segment and will retain them in the region. The effect is stronger for protons with gyration orbit type C than those with gyration orbit type B. Protons of gyration orbit type B could drift out of the filament through cross-field diffusion, similar to the situation shown in panel 1. Protons leaving the segment in the direction along the filament would be suppressed by magnetic mirroring, unlike those in panel 1.

The field configurations in panels 4 and 6 can be considered as continuations of that shown in panel 1, as the strength of $\boldsymbol{B}_{\rm s}$ relative to that of $\boldsymbol{B}_{\rm g}$ increases. This increase will enhance the diffusion of protons with gyration orbit type B out of the filament segment. This in turn reduces the confinement time of these protons. Protons with gyration orbit type C are not affected greatly, unless the corresponding $r_{\rm C}$, the radius of gyration orbit type C, strongly violates the condition:

$$\int_{2\pi/\ell}^{2\pi/r_{\rm C}} {\rm d}^3\boldsymbol{k}\,\left|\tilde{\mathcal{B}}(\boldsymbol{k})\right|^2 \gg \int_{2\pi/r_{\rm C}}^{\infty} {\rm d}^3\boldsymbol{k}\,\left|\tilde{\mathcal{B}}(\boldsymbol{k})\right|^2 , \tag{14}$$

where $\tilde{\boldsymbol{B}}(\boldsymbol{k})$ is given by the Fourier transform:

$$\tilde{\mathcal{B}}(k) \approx \frac{1}{2}\int_{-1}^{1} {\rm d}\mu \int_{0}^{\ell/2} {\rm d}r\, r^2\, \mathcal{B}(\boldsymbol{r})\, e^{-{\rm i}\,\mu k r} \tag{15}$$

for isotropic $\boldsymbol{B}_{\rm s}$.

The magnetic field configuration in panel 5 has the same large-scale field as that in panel 3. The presence of the small-scale disordered field component $\boldsymbol{B}_{\rm s}$ in the magnetic bottle set by the large-scale field component $\boldsymbol{B}_{\rm g}$ will not affect the global confinement of protons with gyration orbit type C. These protons will be reflected back by magnetic mirroring, once they diffuse out from the region with $\boldsymbol{B}_{\rm s}$. The presence of the small-scale disordered field component $\boldsymbol{B}_{\rm s}$ facilitates the diffusion of protons with gyration orbit type B across the filament, where confinement is regulated only by $\boldsymbol{B}_{\rm g}$.

4. Filament Ecology

4.1. Filament Interfaces

Filaments are not isolated structures. They are an integral part of an ecological system for the production, transportation, conversion, and destruction of energetic particles. The

interaction between the filaments and other components in this ecosystem determines the composition, spectrum, and fate of energetic particles. The interfaces of these components are gateways for energetic particles. We may broadly divide these interfaces into three basic classes: filament–void interfaces, filament–cluster/supercluster interfaces, and filament–galaxy interfaces. This classification is not an artificial construct, and we will illustrate that these interfaces act as a sieve for energetic particles entering and exiting filaments.

From a geometrical perspective, interfaces broadly correspond to two magnetic field topologies between three classes of objects of different sizes relative to the size of the filament segments involved: (i) the linear sizes of voids $\ell_{\rm voi} \gg \ell_{\rm fil}$, (ii) the linear sizes of clusters and superclusters[1] $\ell_{\rm cl/sucl} \approx \eta\, \ell_{\rm fil}$ (where $\eta \sim [\mathcal{O}(1)]$), and (iii) the linear sizes of galaxies $\ell_{\rm gal} \ll \ell_{\rm fil}$. Up to this point, we have been using the linear size of a filament segment, ℓ, and the thickness of the filament, $\ell_{\rm fil}$, interchangeably (see Section 3.3) in the context that $\ell \longleftrightarrow \ell_{\rm fil} < \mathcal{C}\ell_{\rm fil}$, where $\mathcal{C} > 1$ is the aspect ratio scaling variable of the filament. These three interface classes are defined by the topological nature of how filaments are associated with the other components in the ecosystem. The properties of interfaces do not follow simple scaling relations according to the sequence of galaxies, cluster/superclusters, and voids. Moreover, we cannot simply scale their physical properties, such as the magnetic field strength and the thermal content of gas according to the characteristic sizes of the component structures. As illustrated in Figure 3, galaxies are enclosed by filaments, and filaments and clusters/superclusters are enclosed by voids; however, clusters/superclusters are linked by filaments.

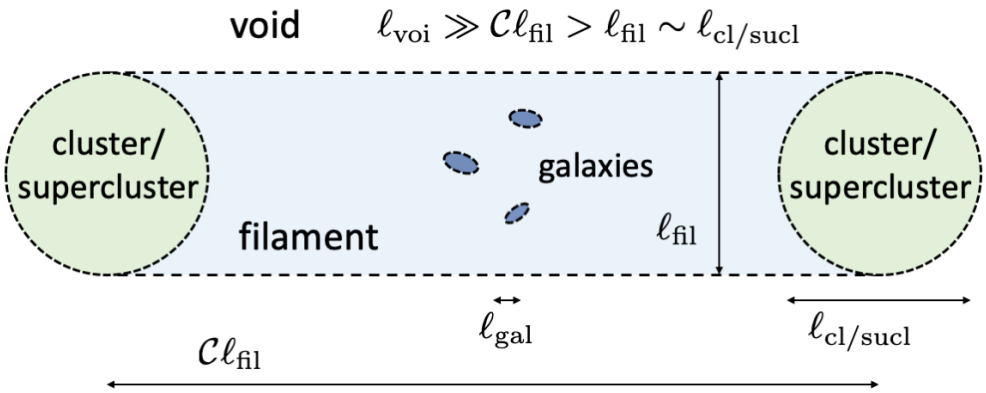

Figure 3. A schematic illustration to show the interfaces of a filament with a void, two clusters/superclusters, and several galaxies embedded in it. The size bars indicating the length scales ℓ_x ($x \in \{\rm fil, voi, cl/sucl, gal\}$) are not exactly to scale. The filament has an elongated shape, hence the filament aspect ratio scaling variable $\mathcal{C} > 1$.

This classification is based on geometrical and topological considerations. The magnetic fields in filaments introduce an additional layer of complexity. If we ignore the magnetic field configurations associated with the interfaces for the time being and adopt the gyration orbits of particles (as described in Section 3.4) as a reference, it can immediately be seen how energetic particles are sieved differently by the three interfaces (which is summarised in Table 1). It is clear that voids can accommodate the most energetic particles (with gyration orbit type A) without difficulty. It is also apparent that filament–void interfaces are a one-way opening for low-energy particles (with gyration orbit type C). These particles can freely enter a filament from a void, but they are unable to break the confinement from a filament to escape to a void. Generally, filaments can accept the particles of gyration orbit type B from galaxies, clusters/superclusters, or voids. Whether these structures can retain particles depends on how far the particles are able to diffuse across the filament before undergoing a hadronic interaction (see Section 2).

Table 1. Passages of cosmic rays through interfaces between filament eco-components.

Interface Type	A	B	C
Void to filament	✗	✓	✓
Filament to void	✓	?	✗
Cluster/supercluster to filament	✗	?	?
Filament to cluster/supercluster	✗	✓	?
Galaxy to filament	✗	✓	?
Filament to galaxy	✗	??	?

Notes: A table to summarise the prospects of particles with given gyration orbits to transfer between filaments and voids, filaments and clusters/superclusters, and filaments and embedded galaxies. A, B, and C correspond to the gyration orbit types A, B, and C in Figure 2. '✓' and '✗' denote which cases could and could not transfer particles via the described pathway, respectively. '?' denotes that transfer through the described pathway is subject to the efficiency of diffusion across the magnetic field, in competition with other relevant processes, e.g., the survival of particles in the presence of pp or $p\gamma$ interactions. '??' denotes that there could be complications in the transfer of particles through the described pathway caused by other factors, such as the presence of a magnetic barrier in the filament–cluster/–supercluster interface, and/or the diffusion of particles through the magnetic field internal to the systems.

Magnetic fields are divergence free, so the open field lines of a filament magnetic field must thread through the interfaces with other eco-components. Figure 4 schematically illustrates examples of the topologies of global, relatively ordered magnetic fields $\boldsymbol{B}_{\rm g}$ associated with the interfaces between a filament segment and a void (panel 1), two clusters/superclusters (panel 2), and several embedded galaxies (panel 3).

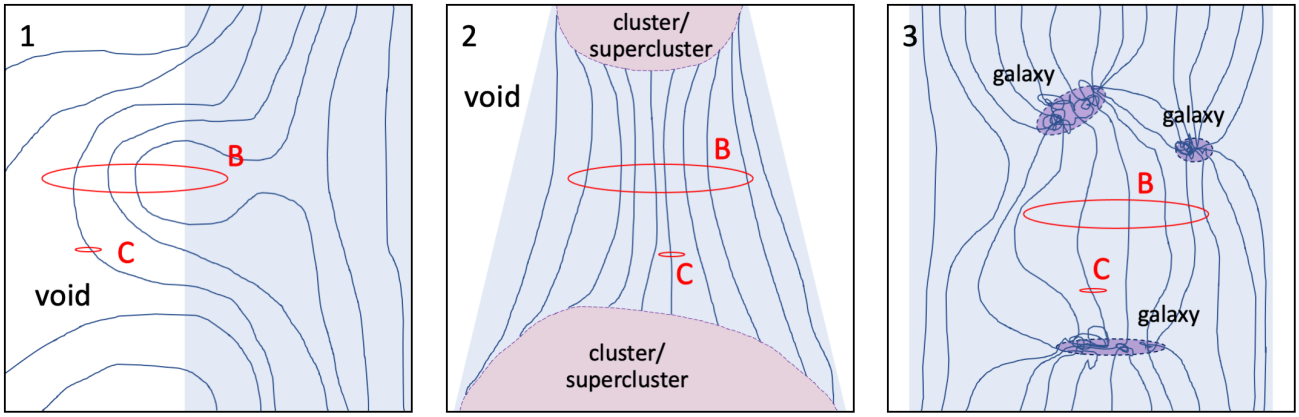

Figure 4. Schematic illustrations of three specific situations for the confinement and propagation of energetic particles in filament environments. Panel 1 shows the closed and open magnetic field lines in the interfacing regions of a filament and a void. Panel 2 shows the filament connecting two clusters/superclusters, where the filament magnetic field lines have a concave configuration (note that we distinguish the filament here from the inter-cluster bridges between two merging galaxy clusters). Panel 3 shows the interweaving structure of magnetic field lines connected between a group of galaxies embedded in a filament. The ellipses B and C are defined as those in Figure 2 (with respect to a characteristic magnetic field and the size of the filament segment considered).

The two kinds of magnetic field topologies associated with filament–void interfaces are open and closed field lines. This is analogous to the magnetic field configuration of stars (see, e.g., [94,95]). In stellar magneto-spheres, closed field lines bound dead zones where charged particles become trapped, while open field lines thread the wind zones where charged particles are allowed to escape. In the filament–void interface (panel 1, Figure 4), particles of gyration orbit types B and C leak out from the filament and will be deflected by the closed magnetic field lines back to the filament (cf. the dead zone in a

stellar magneto-sphere). If the particles leak out from regions threaded by open magnetic field lines, they will continue to drift outwards without confinement (cf. the wind zone in a stellar magneto-sphere). Particles in voids with gyration orbit types B and C can be channelled into filaments when they are magnetically captured, regardless of whether the field line is open or closed.

At the interfaces between a filament and its linked clusters/superclusters, the $\boldsymbol{B}_{g\parallel}$ component should be non-negligible as the open field lines in the filament will terminate there (see illustration in panel 2, Figure 4). Energetic particles could, therefore, drift across the interface along the $\boldsymbol{B}_{g\parallel}$ component from a filament into a cluster/supercluster (or vice versa). The magnetic fields in filaments are of $\sim$10 nG [11,96]. The magnetic fields in the core of clusters have strengths of up to $\sim$10 μG [10,97], but are weaker at their outskirts. The gyration orbit of a particle will, therefore, shrink by almost three orders of magnitude when it enters a cluster from a filament. Particles with gyration orbit type B in a filament can easily be captured by a cluster/supercluster at the interface. By contrast, particles that diffuse from a cluster/supercluster into a filament to end up as particles with a gyration orbit type B would have had much smaller gyration orbits when they were inside the cluster/supercluster.

The magnetic fields at a filament–cluster/–supercluster interface may have some interesting properties based on their topological analysis. The magnetic field at the interface must have a strong toroidal field component perpendicular to $\boldsymbol{B}_{g\parallel}$ and/or a strong smaller scale disordered field component, even if the filament segment linking to the cluster/supercluster lacks a small-scale disordered field component. This can be understood as follows. The linear extent of the interface would be $\ell_{\rm cl/sucl}$, which is of the same order as $\ell_{\rm fil}$. Over this length scale, the strength of the magnetic field would need to increase from 10 nG levels to $\sim$10 μG. The magnetic field energy cannot increase substantially by squeezing or bending $\boldsymbol{B}_{g\parallel}$ in the filament as $\ell_{\rm fil} \sim \ell_{\rm cl/sucl}$. Thus, the options to accommodate this disparity between the field strengths in the filament and the linked cluster/supercluster (if adopting the observed values of filaments and clusters available at the moment) are (i) the presence of a strong toroidal field component (not resulting from deformation of the $\boldsymbol{B}_{g\parallel}$ component), (ii) a strong localised small-scale disordered field component, or (iii) both of these. Whether or not particles would need to overcome this magnetic barrier when entering or exiting the cluster/supercluster would depend on their diffusion and scattering when crossing this barrier. This is not considered in our qualitative analysis using gyration orbits and needs additional consideration in future, more comprehensive modelling studies.

Different from filament–cluster/–supercluster interfaces, the linear extent of the filament–galaxy interfaces is determined by the sizes of the galaxies. It is independent of the thickness of the filament segment containing the galaxies (see panel 3, Figure 4). As the sizes of galaxies are significantly smaller than the thickness of their host filament, i.e., $\ell_{\rm gal} \ll \ell_{\rm fil}$, and galactic magnetic fields (several tens of μG; see [98]) are at least three orders of magnitude stronger than the magnetic fields of filaments (tens of nG [11]), particles with gyration orbit type B in a filament would be captured by galaxies through a ballistic collision instead of a diffusion or a diffusive drift process in the filament magnetic field (regardless of the galactic field configuration). The capture probability of these particle may be estimated as $P_{\rm capture} \sim (\Upsilon/\mathcal{C})(\ell_{\rm gal}/\ell_{\rm fil})^2$, where the structural factor Υ ($\sim\mathcal{O}(1)$) depends on the aspect ratio of the galaxy, and the relative orientation and location of the galaxy in its host filament. For $\ell_{\rm gal} \lesssim 30$ kpc and $\ell_{\rm fil} \sim 2$ Mpc, as $\mathcal{C} > 1$, the capture probability of these filament particles by a galaxy would be well below 1%. Particles with gyration orbit type C in a filament would enter a galaxy through diffusive drift. Their orbit would shrink very significantly after entering the galaxy. Particles with gyration orbit type C originating from an embedded galaxy should have much smaller gyration orbits.

The question now to be asked is whether filament–galaxy interfaces would have similar magnetic barriers to those expected for filament–cluster/–supercluster interfaces, when the filament magnetic fields have a significant non-toroidal large-scale component.

The non-toroidal filament magnetic field, if not bypassing the galaxy, would terminate at the filament–galaxy interface. At the interface, the field lines of these components could connect with local poloidal open field lines or toroidal open field lines from within the galaxy. As an illustration, we may consider a disk galaxy of radius 15 kpc embedded within a filament of thickness 2 Mpc. Suppose there is a magnetic field line bundle with a radius of 0.5 Mpc threaded into an embedded galaxy. The magnetic field strength in the arms of nearby spiral galaxies is ∼10 μG (see, e.g., [98]). It follows that

$$\frac{\Phi_{\rm fil}}{\Phi_{\rm gal}} \sim \left(\frac{10\ {\rm nG}}{10\ \mu{\rm G}}\right)\left(\frac{0.5\ {\rm Mpc}}{15\ {\rm kpc}}\right)^2 \sim 1\ , \tag{16}$$

where $\Phi_{\rm fil}$ is the magnetic flux of the filament magnetic field bundle that threads onto the disk galaxy and $\Phi_{\rm gal}$ is the magnetic flux of the open-line magnetic field from the galaxy. This implies that, unlike the filament–cluster/–supercluster interfaces, filament–galaxy interfaces can easily accommodate filament magnetic fields, even if $\boldsymbol{B}_{\rm g\parallel}$ dominates. If a galaxy has a strong central starburst, the magnetic field in the starburst nucleus could exceed ∼100 μG (see, e.g., [98,99]). Then, the large-scale ordered field of the host filament cannot connect smoothly to the galactic magnetic field. This implies the presence of a toroidal field component and/or a small-scale disordered field component. In this case, a magnetic barrier for the charged particles would be formed, similar to the situation at the filament–cluster/–supercluster interface. We note that this filament interface would also be where the boundary of the CGM is located. If the CGM gas is formed by ejecta from the starburst core of the galaxy, the magnetic fields threaded through it could have a substantial small-scale disordered field component, or perhaps even a toroidal field component.

4.2. Journey, Life Cycle, and Fate of Energetic Particles

The question behind most current studies of the transport of cosmic rays and their interactions is how the medium would affect their transport processes and properties. An ecosystem, however, consists of complex webs of multiply connected components. The question posed above is, therefore, not particularly meaningful, given the multiplicities of energetic particle interactions and the interconnection between the components of the ecosystem that energetic particles would encounter. Posing a grander question of how the web of components associated with cosmic filaments would affect the global transport processes of cosmic rays and the final and intermediate properties of the particles within the components of the system will, however, make the problem impossible to tackle. An alternative approach is to put focus on the individual particles and investigate how they react to the individual components in the system they would encounter. We, therefore, apply the information obtained by studying the journey of individual particles to deduce the life cycle and fate of energetic cosmic rays in filaments and to derive useful insights that can then be applied to the broader astrophysical context.

We start with this question: What will happen to a particle, say a proton, of energy $E_{\rm p}$ starting its journey from a location within a galaxy, a cluster, a supercluster, or a filament at a particular cosmological epoch? Without losing generality, we consider three protons at energies of 10^{12} eV, 10^{16} eV, and 10^{20} eV. The threshold energy for pion production pγ processes in astrophysical environments is above 10^{16}eV (see Section 2). It is considered possible to accelerate particles to energies as high as 10^{20} eV in astrophysical systems, without violating the Hillas criterion [81]. The three energies we have chosen bracket the energy ranges for two regimes: the first is the transport of cosmic rays that do not undergo significant hadronic pγ processes (10^{12}–10^{16} eV), while the second is the transport of cosmic rays that have a possibility to undergo a hadronic pγ process (10^{16}–10^{20} eV). We consider four initial locations for the protons: the filament itself, a very large supercluster, a cluster, and a disk galaxy (which may or may not have starbursts). The assigned characteristic magnetic field strengths are 10 nG for the filament, 1 μG for superclusters and clusters, and 10 μG and 100 μG, respectively, for the disk galaxies with and without starbursts. For

completeness, we also assign a value of 10^{-15} G (=10^{-6} nG) [100,101] for the magnetic fields in voids.

4.2.1. Particles Starting from a Filament

Consider first that the three protons are produced in a filament at the present epoch ($z = 0$). With the assigned filament magnetic field of 10 nG, their Larmor radii $r_{\rm L}$ are 3.33×10^{17} cm ($\sim$0.1 pc) (for 10^{12} eV), 3.33×10^{21} cm ($\sim$1 kpc) (for 10^{16} eV), and 3.33×10^{25} cm ($\sim$10 Mpc) (for 10^{20} eV). The thickness of a filament at the present epoch would be in the range (1–4) Mpc, which is less than 3×10^{25} cm. Thus, only the proton of 10^{20}eV would be able to escape from the filament to the void. The other two would be confined within the filament.

If the 10^{20} eV proton manages to leave the filament and escape into the void, its Larmor radius would be $> 10^{32}$ cm ($\sim 10^4$ Gpc), if we take the magnetic field in the void to be 10^{-15} G (=10^{-6} nG). It practically free-streams away and would not return to the filament it originated from. At the current epoch, it could travel over a distance of a few tens Mpc as collisions with CMB photons degrade its energy through photo-pair and pion production (see Section 2). If its energy drops to around 10^{16} eV, it would still undergo free-streaming propagation as its Larmor radius would be $\sim 10^{28}$ cm ($\approx$3.2 Gpc) $\gg \mathcal{C}\ell_{\rm fil} > \ell_{\rm fil}$. It cannot be captured magnetically by a filament unless it hits it directly, or unless it collides with a gravitational substructure associated with an embedded component of the filament. At the energies $\sim 10^{16}$ eV, the proton cannot undergo pγ processes to produce pions, nor can it lose energy efficiently through any other process. The proton is practically frozen at this energy, wandering in the void. If its energy drops to about 10^{12} eV during a pγ interaction (though this is unlikely, as almost all its energy will be passed to pions in a single collision with a CMB photon), it could then be magnetically captured by a filament, as it would then have a Larmor radius of about 3×10^{24} cm (1 Mpc), i.e., is comparable to $\ell_{\rm fil}$.

A filament-like structure might have begun to appear at redshifts as high as $z \sim 4$, and filaments continue to evolve to become the current form. Energetic protons would respond differently when encountering a filament at $z = 2$ and a modern-day filament, because of filament evolution and the cosmological conditions. A 10^{20} eV proton would have an interaction length of about 10 Mpc at $z = 2$ and a fit more at $z = 0$ (Figure 1) to pγ interactions, and would again lose energy through this process when colliding with a CMB photon. If the proton's energy drops by a factor of 10 through photo-pair and pion production, it can be confined even by a thin filament of a thickness of 1 Mpc. When the proton is deflected back to a filament, it will collide with a photon in the CMB or a local radiation field again until its energy drops below the pγ interaction energy threshold.

Lower energy protons confined in filaments would scatter or diffuse within them, depending on the coherence length scale of the ordered magnetic field. For the case of a cosmic ray proton captured by a cluster, if there is a magnetic barrier as described in Section 4.1 at the filament–cluster interface, it will take additional time to diffuse into the cluster. When protons enter a cluster/supercluster or an embedded galaxy, their Larmor radii will expand roughly according to the scaling $r_{\rm L,x} = r_{\rm L,fil}[(\langle|\boldsymbol{B}|^2\rangle_{\rm x})^{1/2}/\mathcal{B}]$. Here, x $\in$ {gal, cl/sucl} and $\mathcal{B} = (\langle|\boldsymbol{B}|^2\rangle_{\rm fil})^{1/2}$. As the energies of these protons are below the photo-pair and pion production energy thresholds, they will not participate in pγ processes. However, they may lose a small fraction of their energy through the direct production of electron/positron pairs when colliding with CMB photons in the filament. If they are captured by a galaxy (see Figure 5), they may also participate in pp interactions.

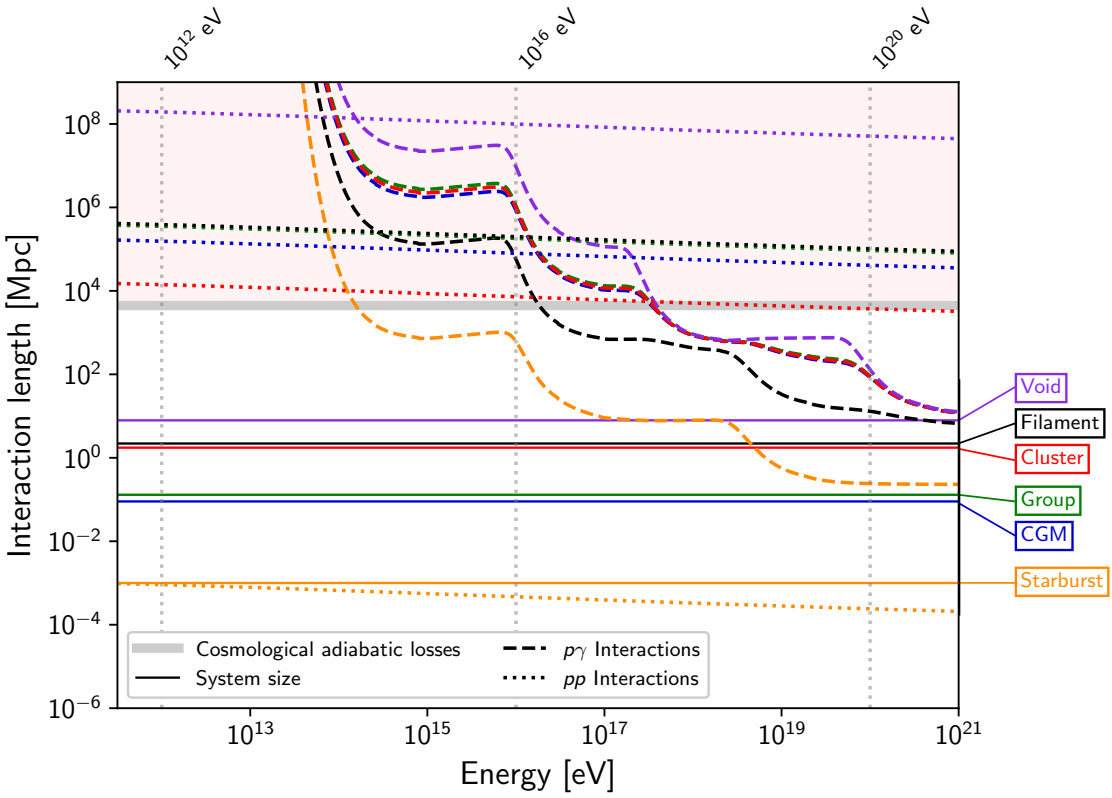

Figure 5. Interaction lengths of protons undergoing pp and pγ interactions in cosmic voids (shown by purple lines), filaments (black lines), and their internal structures: galaxy clusters (shown in red), groups of galaxies (green), the CGM of a galaxy (blue), and a starburst galaxy (orange). All path lengths are calculated at the current epoch ($z = 0$). The length scale for proton adiabatic losses due to cosmological expansion is shown for comparison. Interaction lengths above this scale (indicated by the pink shaded region) are not of astrophysical consequence, but are shown for completeness. The parameters adopted for these calculations are shown in Appendix A, where filament conditions are taken as their central values, while the characteristic size is taken as the filament outskirts, i.e., $\sim$2 Mpc. Vertical lines mark the three proton energies discussed in the main text.

4.2.2. Particles Starting from a Cluster or a Supercluster

For a magnetic field of 1 μG, the Larmor radii of protons with energies of 10^{12} eV, 10^{16} eV, and 10^{20} eV are 3.3×10^{15} cm, 3.3×10^{19} cm ($\sim$10 pc), and 3.3×10^{23} cm ($\sim$0.1 Mpc), respectively. The size of a cluster is a few Mpc, and the linear extent of a supercluster can exceed 100 Mpc.[2]

The sizes of clusters and superclusters are significantly larger than the Larmor radius of the 10^{20} eV proton in μG-level magnetic field strengths. As magnetic field components in clusters or superclusters are expected to have coherence lengths that are smaller than the sizes of clusters/superclusters, the proton with an energy of 10^{20} eV may diffuse out from its host cluster/supercluster into a filament or a void and avoid being captured by a galaxy. This could occur in the current epoch ($z = 0$), as the pγ interaction length for a 10^{20} eV proton is a few tens of Mpc (see Figure 5). The interaction length, however, drops with an increase in redshift, and at $z = 2$, the corresponding pγ interaction length becomes smaller than 1 Mpc, implying that photo-pair and pion production arising in collisions with CMB photons can substantially degrade the energy of the proton. The proton may still leak out from a cluster with a size of a few Mpc, but it is unlikely to be able to escape intact from a supercluster with a size of 100 Mpc.

The two protons with lower energies of 10^{12} and 10^{16} eV would be trapped within their cluster/supercluster of origin. Their energies are below the pγ interaction energy threshold

(see Figure 5), so they practically become fossilised at this energy with pair-production being unable to cool them rapidly. However, the Larmor radii of these protons is sufficiently small that they could become entangled and advected by cluster-scale flows (e.g., in mergers), or in strong AGN outflows, or AGN-induced large-scale bubbles. Otherwise, they will diffuse around until being captured by a galaxy within the cluster/supercluster.

4.2.3. Particles Starting from a Disk Galaxy

Observations have shown that the magnetic fields of disk galaxies often have a relatively well-ordered pattern (e.g., [87,98,103]). In a magnetic field of 10 μG, protons with energies of 10^{12} eV, 10^{16} eV, and 10^{20} eV have Larmor radii of 3.3×10^{14} cm, 3.3×10^{18} cm ($\sim$1 pc), and 3.3×10^{22} cm ($\sim$10 kpc), respectively. The diameter of a Milky Way-like galaxy is about 30 kpc, and the scale-height of the galactic disk would be about $(1-2)$ kpc (see, e.g., [104,105]).

A 10^{20} eV proton, if they are produced in violent environments, such as from a gamma-ray burst (see, e.g., [106]), an AGN (see, e.g., [107]), or even a weakly accreting black hole, could easily stream out of the galactic disk, unless it first collides with an ISM baryon or a photon from the radiation field of some bright stellar objects. The pγ interaction length of 10^{20} eV protons is significantly larger than the diameter of the galaxy; hence, there is little chance it can collide with a CMB photon before leaving its galaxy of origin. The final destination of this fugitive proton, which retains its energy, may be in a cluster, a supercluster, or a filament, and its fate will be similar to the respective 10^{20} eV protons as described in Sections 4.2.1 and 4.2.3. The lower energy protons will be confined by the disk magnetic field and end up undergoing a pp interaction when colliding with a baryon, or a pγ interaction when colliding with a photon from the stellar radiation field.

The situation would be different if the disk galaxy has a strong outflow driven by the starburst (see, e.g., [108]) from within. First, these galaxies may have a stronger magnetic field (see [98]). Second, disk galaxies with strong outflows would have a different topology from disk galaxies without an outflow, especially in the presence of large-scale open field lines, which extend into the galactic halo (see, e.g., NGC 4631, NGC 891, and M 82 [109–111]). For a magnetic field of 100 μG, the Larmor radii of protons with energies of 10^{12} eV, 10^{16} eV, and 10^{20} eV are 3.3×10^{13} cm, 3.3×10^{17} cm ($\sim$0.1 pc), and 3.3×10^{21} cm ($\sim$1 kpc), respectively. A proton with an energy of 10^{20} eV would be scattered by the galactic magnetic field and leave the galaxy, provided it survives pion-producing hadronic collisions with ambient baryons or photons. The fate of this proton is similar to its corresponding fugitive proton from the disk galaxy without an outflow. The proton with an energy of of 10^{16} eV and of 10^{12} eV could be advected out of the galaxy, practically intact, if it is entangled in the magnetic field carried by the outflow. Otherwise, the proton of such a low energy will reside within its galaxy of origin until it collides with a baryon and lose its energy in the particle production cascades (see Figure 5).

5. Astrophysical Implications

5.1. Filaments as Cosmic Ray Highways and Fly Papers

The ability of filaments to retain energetic particles gives them a very special role in the transfer of cosmic rays on a cosmological scale. In most current studies of cosmological-scale cosmic ray transport, all material outside galaxies is broadly referred to as the "IGM". This is treated as a single static agent, with which cosmic rays interact as they propagate through the Universe. This "IGM" is generally described in terms of certain variables in a statistical manner, which are either inferred from observations or extrapolated from simulations.

In the previous section, we demonstrated that energetic protons starting from galaxies, clusters, superclusters, and filaments each have a different life journeys, marked by their identity. Their fate depends on where they come from, where they were born, and how much energy they initially acquired. With a qualitative, heuristic analysis of the journey and fate of energetic protons originating from a filament, a cluster and a supercluster linked to a filament, and a galaxy embedded inside a filament, we have been able to derive insights

into various aspects of cosmic ray ecology within filament environments. Filaments are special large-scale structures that have direct contact with all key eco-components-voids, cluster/superclusters, and galaxies. This connectedness implies that filaments play an important role in mediating and regulating cosmological cosmic ray transfer in a manner that has much more physical complexity than a simple diffusion/scattering scenario can easily accommodate.

Our analysis has shown that filaments are cosmological-scale highways that confine cosmic rays and channel them between clusters, superclusters, and galaxies. An energetic particle escaping from a cluster is not expected to have a good chance to ballistically hit a neighbouring cluster when it is free-streaming in vast inter-cluster space where the magnetic fields are weak (below $\sim 10^{-15}$ G in cosmic voids). However, if the energetic particle enters a filament, it will be magnetically channelled towards another cluster at the other end of the linking filament. The situation is the same for cosmic ray particles leaving a galaxy or a galaxy group embedded within a filament. These are channelled towards nodes as their destinations[3].

Voids enclose filaments, and filaments cannot serve as highways to channel cosmic rays across void–filament interfaces. Cosmic rays breaking filament confinement would have a Larmor radius larger than the thickness of a filament. As such, they would be scattered when they encounter another filament along their path (e.g., [113,114]). These cosmic rays need to undergo a 'transformation' before they can be captured and retained by a filament. Cosmic ray protons with energies above the pγ interaction threshold can degrade to become lower energy protons through their collisions with CMB photons. When their energies drop to $\sim 10^{18}$ eV, their Larmor radii $r_{\rm L}$ will be $\sim 3 \times 10^{23}$cm ($\approx$100 kpc) for a magnetic field of $|\boldsymbol{B}| \approx 10\,$nG. A 10^{18} eV proton can then be magnetically captured when intercepted by a filament. This means that filaments can act as cosmic ray 'fly paper', targeting lower energy particles. Given that the volume filling factor of filaments in the Universe is estimated to be about 10% (see, e.g., [115]), the chance of a streaming cosmic ray to collide with a filament is not negligible. Once a cosmic ray has been captured by a filament, it can then undergo pγ interactions inside, degrading its energy to a few 10^{16} eV. These captured cosmic rays will eventually become frozen at some energy $\lesssim 10^{16}$ eV over the timescale it takes them to traverse the filament.

5.2. Cumulative Calorimetry

The fact that protons with energies of 10^{18} eV can be magnetically confined in filaments and that protons of energy below 10^{16} eV do not lose energy rapidly through pγ processes produces some interesting consequences in filament environments. We illustrate schematically the transfer of cosmic rays in filament environments in Figure 6. From this illustration, we can construct a mathematical model to determine the populations of cosmic ray protons in the energy range 10^{12}–10^{16} eV within filaments and voids.

Without loss of generality, we consider an idealistic model as an illustration. It is expressed mathematically in terms of two coupled first-order differential equations:

$$\frac{\mathrm{d}\, n_{\rm fil}}{\mathrm{d}\, t} = -\alpha_{\rm a}\, n_{\rm fil} + \alpha_b n_{\rm voi} + j_{\rm inj} + j_{\rm con,a}\ ; \tag{17}$$

$$\frac{\mathrm{d}\, n_{\rm voi}}{\mathrm{d}\, t} = -\alpha_{\rm b}\, n_{\rm voi} + j_{\rm cov,b}\ , \tag{18}$$

where $n_{\rm fil}$ and $n_{\rm voi}$ are the number densities of cosmic ray protons in filaments and voids, respectively. The coefficients $\alpha_{\rm a}$ and $\alpha_{\rm b}$ represent the rate cosmic ray protons are channelled out of filaments and the rate cosmic ray protons from voids are captured by filaments. For filaments, the rate of injection of cosmic ray protons into the 10^{12}–10^{16} eV energy range is specified by $j_{\rm inj} + j_{\rm con,a}$. Here, $j_{\rm inj}$ accounts for contributions from direct injection by galaxies (and galaxy groups), clusters, superclusters, and filament shocks (if present). $j_{\rm con,a}$ is the contribution from protons at higher energies that are converted into the 10^{12}–10^{16} eV energy range by pγ processes in filaments. In voids, this conversion process is specified as

$j_{\rm con,b}$. Therefore, this conversion process tends to dominate cosmic ray injection into the 10^{12}–10^{16} eV energy range.

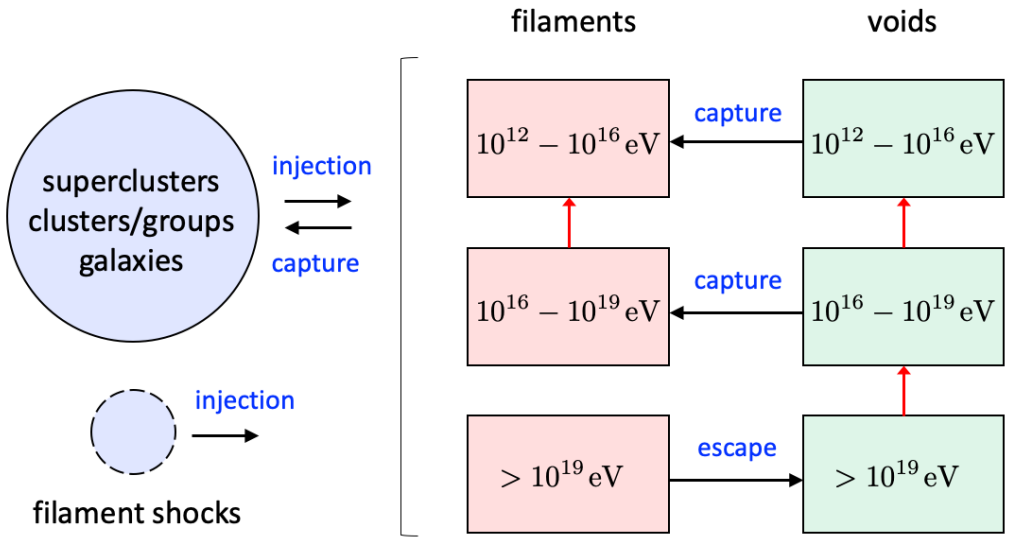

Figure 6. A schematic illustration of the transfer of cosmic ray protons in filament and void environments. The protons are sorted into three broad groups of energy $>10^{19}$ eV, $10^{16}-10^{19}$ eV, and 10^{12}–10^{16} eV. The horizontal arrows denote the transfer of the particles in the context of relocation from one astrophysical system to another. The vertical red arrows denote the conversion of cosmic ray protons from a higher energy group to a lower energy group through pγ processes.

In general, $j_{\rm conv,a}$ and $j_{\rm conv,b}$ are time-dependent. Their evolution is determined by the cosmic ray energy spectrum, the cosmic ray population, and local radiation fields. By contrast, $j_{\rm inj}$ is determined by the star-formation and active galactic nucleus activities at a given cosmological epoch. This implies that $\alpha_{\rm b}\, n_{\rm fil}$ is also time-dependent, even without consideration of the structural evolution of filaments and the cosmological expansion of voids. Nonetheless, as the capture of cosmic ray protons in filaments by lower ordered structures would not be high, and as cosmic ray protons are not expected to show an upturn in their spectra for energies above 10^{19} eV, it is reasonable to expect that $j_{\rm inj} > j_{\rm con,a} \gg |\alpha_b n_{\rm voi} - \alpha_{\rm a}\, n_{\rm fil}|$, and $j_{\rm con,b} > \alpha_{\rm b} n_{\rm voi}$, at least during the epochs when star-formation and AGN activity peaked (roughly at $z \approx 2$). If we keep only the dominant terms, the cosmic ray transfer equations are decoupled, giving a solution:

$$n_{\rm fil} \approx \int_{z_{\rm AGN,0}}^{0} {\rm d}z \left(\frac{{\rm d}z}{{\rm d}t}\right)^{-1} \varpi(z)\, j_{\rm int}(z)\, \theta(z - z_{\rm fil,0}) + \int_{z_{\rm gal,0}}^{0} {\rm d}z \left(\frac{{\rm d}z}{{\rm d}t}\right)^{-1} [1 - \varpi(z)]\, j_{\rm int}(z)\, \theta(z - z_{\rm fil,0})\,; \quad (19)$$

$$n_{\rm voi} \approx \int_{z_{\rm max}}^{0} {\rm d}z \left(\frac{{\rm d}z}{{\rm d}t}\right)^{-1} \varkappa(z)\, j_{\rm int}(z)\,, \quad (20)$$

where $\theta(\cdots)$ is a Heaviside step function. The redshifts $z_{\rm AGN,0}$, $z_{\rm gal,0}$, and $z_{\rm fil,0}$ denote the epoch of emergence of the first AGN, the first star-forming galaxies, and the first cosmological filaments, respectively, and $z_{\rm max} = {\rm Max}(z_{\rm gal,0}, z_{\rm AGN,0})$. The ratio of relative contributions of cosmic ray injection by star formation to that by AGN activities at redshift z is specified by by $[1 - \varpi(z)]/\varpi(z)$. The scaling for protons with energies above the pγ interaction threshold at redshift z leaking into the cosmic void is specified by $\varkappa(z)$.

While this set of solutions does not capture all of the fine details of the evolution of a population of cosmic ray protons in the energy range 10^{12}–10^{16} eV, it still gives us some useful insights into the history of the cosmic ray content of filaments and voids. As $({\rm d}z/{\rm d}t)$ is negative while all the other terms in the integrand are positive, $n_{\rm fil}$ and $n_{\rm voi}$

would increase over time until reaching a saturation level, where the injection and leaking of cosmic ray protons in filaments and voids fall into a steady balance. Filaments and voids would, therefore, continue to accumulate cosmic ray protons in this energy range, provided that their injection rate is higher than their loss rate through leaking into lower ordered cosmological structures, or through subatomic processes such as pair production. This implies that, compared to galaxies (and groups), clusters, and superclusters, cosmic rays in filaments and voids would have a stronger component of protons at energies around 10^{16} eV, which are unable to cool efficiently and do not undergo pγ processes. Filaments cannot be populated by cosmic ray protons with energies greatly exceeding 10^{17} eV, because they will be depleted by interactions with photons in the local and cosmological radiation fields. They also cannot be greatly populated by cosmic ray protons at energies far below 10^{12} eV, as these would be magnetically confined by the galaxies, clusters, or superclusters from where they originate and cannot migrate out into filaments and voids.

5.3. Some Remarks

5.3.1. Cosmic Ray Energy Density and Energy Partition with Magnetic Fields

The large population of cosmic rays with energies 10^{12}–10^{16} eV in filaments and voids result from previous star-forming and AGN activities in the Universe. Their presence has some consequences for how we interpret observations of the micro-physics in filaments and voids. Firstly, the spectrum of cosmic rays observed on Earth and the spectrum of galactic cosmic rays are not representative of the spectrum in filaments and voids. Secondly, without reliable information about the cosmic ray spectrum in intergalactic space, caution is needed when deriving certain properties of filaments and voids based on the assumed number density and energy spectra of cosmic rays, for example when estimating filament and void magnetism.

In the two-component deposition of the filament magnetic field, the two orthogonal sub-components of the large-scale ordered field component are $\boldsymbol{B}_\mathrm{g} = \boldsymbol{B}_\parallel + \boldsymbol{B}_\phi$, where $\boldsymbol{B}_\parallel$ is aligned with filament and $\boldsymbol{B}_\phi$ is the toroidal field component perpendicular to $\boldsymbol{B}_\parallel$. Including also the small-scale disordered field component, the magnetic energy density in the IGM within a filament would be

$$\langle \epsilon_B \rangle = \frac{1}{8\pi}\Big(\langle {B_\parallel}^2 \rangle + \langle {B_\phi}^2 \rangle + \langle {B_\mathrm{s}}^2 \rangle \Big) \tag{21}$$

(assuming that the large-scale and the disordered components are linearly independent). Unless there is strong co-evolution of $\langle \epsilon_\mathrm{B} \rangle$ and n_fil, it is not obvious how a relation can be established between $\langle \epsilon_B \rangle$ and $n_\mathrm{fil} \langle \mathcal{E}_\mathrm{p} \rangle$, where $\langle \mathcal{E}_\mathrm{p} \rangle$ is the energy content per cosmic ray particle in the energy range 10^{12}–10^{16} eV. Also, whether or not energy equipartition $\langle \epsilon_B \rangle = n_\mathrm{fil} \langle \mathcal{E}_\mathrm{p} \rangle$ can be attained uniformly over a length scale comparable to the linear sizes of filaments or voids is beyond our current knowledge.

5.3.2. Cosmic Ray Transfer on Cosmological Scales

Treating the magnetised IGM as a uniform static medium gives tremendous simplification when mathematically formulating cosmic ray transfer. One advantage is that we may classify different transport regimes based on the statistical properties of the IGM, and this makes solving the transfer equations tractable. However, the disadvantage with this approach is that it fails to account for the complexities in the cosmic ray transfer process, such as expanding-volume, multi-scale (but non-turbulent) structures. As shown in the case studies of the journey and fate of individual cosmic ray protons at different energies, the regime-based solution schemes using the average statistical properties of the of IGM do not immediately give a reliable description of the cosmic ray properties in filaments and voids. It is also not easy to incorporate the conversion of particles and the sudden jump in the characteristic scales involved when cosmic rays are transferred from one cosmological component to another, in the coexistence of deterministic and stochastic chance encounters.

The heterogeneity of the medium over which cosmic rays propagate and the capture of cosmic rays by strongly magnetised substructures are subjects of concern on galactic scales. Studies have been conducted on quantifying how cosmic rays are transferred in media with intermittent patchy structures (see, e.g., [116,117]) and in the presence of random magnetic traps [118]. The challenges of cosmic ray transport on cosmological scales share some similarity with those within the ISM of galaxies, but there are also additional layers of complexity inherent from the different natures between cosmological environments and sub-galactic environments. The first is how the presence of interfaces between systems (see Section 4.1) can play a role[4]. The second is the operation of the sieve mechanism in filament environments, in particular how the conversion of particles will alter the transmission of cosmic rays across the interfaces.

The traditional mathematical formulations for diffusion and scattering are insufficient to describe cosmic ray transfer in filament environments. Mathematical formulations of this kind generally give solutions in terms of a Brownian random walk, or a modified version of it (see, e.g., [119]). The presence of a long tail in the free-path distribution when cosmic rays propagate through the vast intergalactic space cast by an interweaving web of filaments (see, e.g., [120]) implies that the underlying process is Levy flight (see, e.g., [121,122]), rather than Brownian motion. With appropriate modifications, the Levy flight formulation would be able to handle complexities arising from interface-induced barrier crossing (cf. [123]) and chance conversion/elimination of particles [124]. Constructing and solving cosmic ray transfer equations with a Levy flight formulation is beyond the scope of this study (see also [125]), and we shall present our work on this in a series of future papers.

5.3.3. The Cosmic Rays That Will Never Reach Us

Our analysis has demonstrated the presence of a large population of cosmic ray protons in filaments in the energy range of 10^{12}–10^{16} eV. In a filament with a characteristic magnetic field $\mathcal{B} \sim 10$ nG, the synchrotron cooling timescales are about 2.2 Gyr and 220 Gyr for protons with energies 10^{12} eV and 10^{16} eV, respectively, adopting the expression for proton synchrotron cooling time in [126]. Thus, there would be a pile-up of energetic protons above 10^{12} eV over time. In a void with a magnetic field of 10^{-6} nG, the synchrotron cooling time of these protons is many orders greater than the Hubble time. These wandering protons in comic voids with energies below the pγ threshold, therefore, become fossilised after their last hadronic interaction.

Given the large combined volume occupied by voids and filaments (excluding galaxies, clusters and superclusters), the total number of cosmic ray protons and the amount of energy they store would be substantial. As these hidden particles have derived their energies from star-formation and AGN activities, they are fossil records of the power generation history of the Universe (after the emergence of the first stars, first galaxies, and first quasars).

The cosmic ray spectrum observed on Earth is characterised by features such as the ankle and knees (see, e.g., [127]). A simple interpretation (as illustrated schematically by [128]) is that the cosmic rays are dominated by three components. The knees at energies below a few 10^{17} eV are signatures of the two lower energy components, which are of galactic origin, contributed mainly by supernova remnants. The ankle is caused by the transition from the two lower energy components to a high-energy component. It is commonly attributed to cosmic rays originating from outside the Milky Way (for a review, see [129]). The extragalactic component has a low-energy drop-off, as cosmic rays with energies below $\sim 10^{16}$ eV from outside the Milky Way are expected to be strongly deflected by galactic magnetic fields. The observed cosmic ray spectrum on Earth implies that galaxies like the Milky Way will censor the direct detection of of the fossil cosmic ray proton populations, even if these protons manage to leave the filaments and voids they had previously resided in. In other words, these cosmic rays will never reach us.

The cosmic ray spectrum observed on Earth is a consequence of a dynamical equilibrium of cosmic ray transfer from galactic and extragalactic origins. The spectral properties

reflect the 'now', situation of the cosmic ray properties around the Earth, and the synchronisation of the evolution of the cosmic ray spectrum with cosmic ray production, transport, conversion and destruction in the nearby Universe. The spectral properties of the cosmic ray population of energies 10^{12}–10^{16} eV in filaments and voids are, by contrast, the result of a dynamical equilibrium. This cosmic ray population is evolving with the Universe. Their cumulative nature implies that they retain memory of past events (see Equations (19) and (20)), such as the epochs when star-forming and AGN activities in the Universe peaked, and the continual reconfiguration of the cosmic web woven by large-scale filaments.

6. Conclusions

In this work, we have demonstrated the importance of cosmological filaments in the transport and entrapment of energetic hadronic cosmic rays. We have found that the interplay of energy-dependent particle transport and hadronic interaction processes produces a range of evolutionary paths for the cosmic rays depending on their energy and location of origin. In particular, two regimes emerge in which cosmic rays engage differently with filament ecosystems. At low energies, they undergo transport, but are below the threshold energy for pion production processes. Without any other efficient cooling process available for them, the evolution of these cosmic rays is regulated by the magnetic configuration of filament ecosystems, with their energy becoming 'frozen'.

At higher energies, above the pion production threshold, cosmic rays degrade in energy via interactions with cosmological and local radiation fields as they propagate. These interacting cosmic rays can generally escape from magnetised structures embedded within filaments, but only some may be able to diffuse out of the large filaments and into cosmic voids. They lose energy quickly through pion production, and soon fall below the interaction threshold energy. They then join the fossil population of non-interacting cosmic rays in voids and filaments.

The exact fate of cosmic rays depends on their location of birth. If originating from a cluster or galaxy, only the most energetic cosmic rays have a chance to diffuse out. Lower energy cosmic rays are trapped in their cluster or galaxy of origin. If originating from a filament, only the highest energy cosmic rays can escape. Those below 10^{18} eV are confined by the filament to scatter and diffuse inside it. The filament then operates as a cosmic ray highway, channelling the entrapped particles along it. Those cosmic rays that do escape lose energy in the void by pion production until they fall below the interaction threshold. Unless these fugitive cosmic rays are captured by a filament while they shed their energy, they are left to wander in the void. Unable to cool efficiently, they form a relic ocean of void-filling cosmic rays. They can only leave the void by colliding directly with a filament or one of its gravitationally bound substructures where the stronger magnetic fields can capture them.

Overall, our findings point towards a build-up of a cosmic ray ocean in the 10^{12}–10^{16} eV energy range within voids and filaments. At higher energies, cosmic ray populations are depleted by interactions with photons in local and cosmological radiation fields. At lower energies, cosmic rays can be magnetically confined by the galaxies, clusters, or superclusters from where they originate, and cannot migrate out into filaments and voids. This ocean of relic cosmic rays in filaments and voids develops to harbour a substantial energy component in the Universe. Their exact spectral properties and cumulative evolution become a long-lived 'fossil' population that records the power generation history of the Universe and the evolution of the cosmic web. Yet, as they would be strongly deflected by the magnetic fields of galaxies like the Milky Way, this vast population of relic cosmic rays will never reach us, even if they are able to escape from their structure of origin.

Author Contributions: All authors contributed to the scientific content of this article. Conceptualization, K.W. and L.L.; Methodology, K.W., E.R.O. and Y.I.; Validation, Q.H. and Y.I.; Formal analysis, K.W., E.R.O. and Q.H.; Investigation, K.W., E.R.O., Q.H., Y.I. and L.L.; Writing—original draft, K.W. and E.R.O.; Writing—review and editing, Q.H. and Y.I.; Supervision, K.W. All authors have read and agreed to the published version of the manuscript.

Funding: K.W. and Q.H. acknowledge support from the UCL Cosmoparticle Initiative. Q.H. is supported by a UCL Overseas Research Scholarship. Q.H. and L.L. are supported by a UK Science and Technology Facilities Council Research Studentship. E.R.O. is an overseas researcher supported by a Postdoctoral Fellowship of the Japan Society for the Promotion of Science (JSPS KAKENHI Grant Number JP22F22327). Y.I. is supported by an NAOJ ALMA Scientific Research Grant Number 2021-17A, JSPS KAKENHI Grant Numbers JP18H05458, JP19K14772, and JP22K18277, and the World Premier International Research Center Initiative (WPI), MEXT, Japan.

Data Availability Statement: Data are contained within the article.

Acknowledgments: This work made use of the NASA Astrophysics Data System (ADS).

Conflicts of Interest: The authors declare no conflicts of interest.

Abbreviations

The following abbreviations are used in this manuscript:

AGN	active galactic nuclei/nucleus
CGM	circumgalactic medium
CMB	cosmic microwave background
GZK	Greisen–Zatsepin–Kuzmin
ICM	intra-cluster medium
IGM	intergalactic medium
IR	infra-red
ISM	interstellar medium
ΛCDM	Lambda Cold Dark Matter
RM	rotation measure
UHE	ultra-high energy
WHIM	warm–hot intergalactic media/medium
EBL	extragalactic background light
FUV	far-ultraviolet
HCG	Hickson Compact Group
HyLIRG	hyper-luminous infra-red galaxy
ISRF	interstellar radiation field
IGrM	intra-group medium

Appendix A

Table A1. Summary of the parameters adopted in our calculations for the hadronic pp and pγ path lengths shown in Figure 1, for filament and void conditions. In all cases, pγ interactions with the CMB at the specified redshift are included in our calculations.

Environment	Redshift	Radiation Energy Density [eV cm^{-3}]		Gas Density [g cm^{-3}]	Size [h] [Mpc]
		Starlight	Dust		
Central filament [a]	0	3.7	5.2	4.0×10^{-29}	0.30
	2	28	42	3.6×10^{-28}	0.20
	7	3.4	4.7	2.0×10^{-26}	<0.050
Filament outskirts [a]	0	0.10	0.14	1.4×10^{-30}	2.0
	2	0.076	1.1	1.3×10^{-29}	2.5
	7	0.091	0.13	7.0×10^{-28}	>2.8
Void [b]	0	0.022	0.032	8.0×10^{-32}	7.9
	2	0.17	0.25	1.4×10^{-30}	6.7
	7	0.021	0.028	7.6×10^{-29}	6.0
Average IGM [c]	0	0.024	0.035	4.0×10^{-31}	–
	2	0.19	0.29	3.6×10^{-30}	–
	7	0.023	0.031	2.0×10^{-28}	–
Starburst galaxy [d]	0	670	310	1.7×10^{-20}	0.0010
CGM [e]	0	0.24	0.34	1.0×10^{-28}	0.10

Table A1. *Cont.*

Environment	Redshift	Radiation Energy Density [eV cm^{-3}] Starlight	Dust	Gas Density [g cm^{-3}]	Size [h] [Mpc]
Intra-group medium [f]	0	0.22	0.31	4.4×10^{-28}	0.12
Intra-cluster medium [g]	0	0.21	0.28	1.1×10^{-27}	1.9

Notes: [a] Filament gas density estimates are based on the structural classification proposed by Ref. [130], where central filaments have an overdensity of 100, and filament outskirts have an overdensity of 3.5 compared to the average background IGM. Central densities are typically 5–15-times the critical density of the Universe at all redshifts. The energy densities of filament radiation fields follow the total stellar and dust contributions to the extragalactic background light (EBL) at $z = 0$ in Ref. [49]. These are modelled as modified black bodies, with characteristic temperatures of 7100 K (starlight) and 62 K (dust), following the dominant components of the EBL. Radiation energy densities in filaments at higher redshifts are obtained by scaling the $z = 0$ EBL values with the cosmic star-formation rate density [131], as obtained from FUV and IR data for the stellar and dust EBL components, respectively. Within filaments, radiation fields are scaled by the excess stellar density for long filaments in Ref. [132], corresponding to an increase by a factor of 150 in central filaments, and by 4 in filament outskirts. [b] Void densities $\rho_{\rm voi}$ are estimated from typical density contrasts of $\rho_{\rm voi}/\rho_{\rm B} \sim 0.20$ at $z = 0$ and 0.38 at $z = 2$ compared to the background average IGM density $\rho_{\rm B}$ [133]. An estimate for the void density contrast is unavailable at $z = 7$. Given that void density contrasts are weaker at higher redshifts, we applied the $z = 2$ contrast to ensure our path length calculations are conservative. Our estimated void densities are a factor of ∼10–100 lower than the critical density at all redshifts. The reduction of the EBL due to the presence of a void is not substantial. Following Ref. [134], we assume a 10 percent reduction compared to the average EBL energy density. This is conservative and corresponds to voids of sizes 100 h^{-1} Mpc, which have the lowest EBL levels. The ΛCDM model of Ref. [135] is adopted for the redshift evolution of cosmic void sizes. [c] The comoving cosmic mean baryon density reported by Ref. [5] is adopted as the average IGM density at $z = 0$. Values at higher redshifts are scaled from the $z = 0$ density by cosmological volume. [d] Parameters are informed by conditions in the nearby hyper-luminous IR starburst galaxy (HyLIRG) IRAS F14537+1950, where the interstellar radiation field (ISRF) intensity is scaled by bolometric luminosity compared to the galaxy, from [136]. F14537+1950 has a redshift of $z = 0.64$ with no indication of AGN activity [136]. This is chosen as an extreme example of a low-redshift starburst galaxy. To allow for direct comparison with the other structures, our path length calculations assume $z = 0$, rather than the measured redshift of this galaxy. The external EBL contribution is negligible. [e] Gas density estimated from the mean CAMELS-IllustrisTNG profiles in Ref. [137] at a radius of 0.1 Mpc for galaxies of halo mass between 10^{12} $M_\odot$ and $10^{12.3}$ $M_\odot$. At this radius, feedback effects do not have a large impact on the density profile. Radiation field energy densities are estimated by scaling the dust emission from the ISM of the starburst galaxy IRAS F14537+1950 by the square of the relative sizes of the systems. This assumes that most stellar radiation in a starburst galaxy is re-radiated in the IR band by dust. The starlight is then scaled from this by the relative energy density ratio of the EBL. An additional contribution from the average external IGM EBL is included in the CGM radiation field. [f] Properties of groups of galaxies show broad variation. We adopted the average properties of the sample of galaxy groups from Ref. [138] (see the r_{500} values in their Table 1a) as a representative example of the density of the intra-group medium (IGrM) (for a review of properties of the IGrM, see Ref. [139]; characteristic physical/observable properties of galaxy compact groups; see Ref. [140]). For the intra-group light (IGrL), we estimated the dust contribution using the total IR luminosity of the Hickson Compact Group (HCG) 40 group members in [140] (see their Table 4) and separations (their Table 6), adopting a five-member configuration. The stellar contribution is then scaled from the dust contribution according to the ratio of starlight to dust luminosities reported for the EBL at $z = 0$. An additional contribution from the average IGM EBL is included in the IGrL radiation field, which permeates the system. [g] The density of the intra-cluster medium is based on the average of the sample of clusters presented in Ref. [138] (see the r_{500} values in their Table 1b). This value corresponds to ∼130-times the critical density of the Universe at $z = 0$. When accounting for the uncertainties in the sample, this overdensity is comparable to that typically adopted for galaxy clusters, where a value of ∼200 has been shown by N-body simulations to correspond to the virialised region of a cluster's dark matter halo (see [141]). Radiation energy densities are considered to be double those of the filament outskirts, roughly following the increase in radiation fields shown in Ref. [142], if estimating characteristic values from the Virgo cluster. This is conservative to ensure that cosmic ray interaction rates are not overstated in our calculations. Note that the adopted values are lower than in central filaments, as they are an average value over the cluster. In central cluster regions, radiation fields may be comparable to or could even exceed those of the central regions of filaments. The contribution from the external EBL is intrinsically included by our approach. [h] Characteristic proper widths of filaments are obtained from Ref. [20], which provides density profiles up to $z = 4$ showing the collapse and contraction of the filament profile. At $z = 7$, the result at $z = 4$ is taken as a limit. The central filament is considered to be the region where gas densities in Ref. [20] are 100-times the background IGM average density, while the outskirts are considered to be 3.5-times higher than the background IGM. Void sizes are estimated by invoking spherical morphologies to convert characteristic proper volumes reported for the ΛCDM model of Ref. [135] to proper void diameters, assuming a Hubble parameter of $h = 0.7$.

Notes

[1] Galaxy clusters are not all virialised objects (see, e.g., [92]), and superclusters are not virialised. Superclusters cannot be described by simple geometrical shapes, such as spheres or ellipses. For example, the Laniakea Supercluster [93] does not have a well-defined shape. It is elongated, and presumably threaded by many filaments at different locations. The term 'linear size' of the cluster and supercluster here is, therefore, used in a loose context.

[2] The Laniakea supercluster and the Saraswati supercluster are among the biggest known superclusters to date. They are estimated to have a (maximum) linear extent of $\sim$160 Mpc [93] and $>$ 200 Mpc [102], respectively.

[3] Apart from clusters and superclusters, galaxy groups can also serve as nodes of large-scale filaments. In a recent observation, the M 101 galaxy group was identified as a node in a nearby cosmic filament [112].

[4] This is analogous to determining the electric and magnetic fields in propagating electromagnetic waves across two dielectric media with different refractive indices. The matching of the field components at the boundary is essential to obtain a correct description of the transmission and reflection of electromagnetic waves when crossing the interface between the two media.

References

1. Eckert, D.; Jauzac, M.; Shan, H.; Kneib, J.P.; Erben, T.; Israel, H.; Jullo, E.; Klein, M.; Massey, R.; Richard, J.; et al. Warm-hot baryons comprise 5–10 per cent of filaments in the cosmic web. *Nature* **2015**, *528*, 105–107. [CrossRef]
2. Vernstrom, T.; Heald, G.; Vazza, F.; Galvin, T.J.; West, J.L.; Locatelli, N.; Fornengo, N.; Pinetti, E. Discovery of magnetic fields along stacked cosmic filaments as revealed by radio and X-ray emission. *Mon. Not. R. Astron. Soc.* **2021**, *505*, 4178–4196. [CrossRef]
3. Tanimura, H.; Aghanim, N.; Kolodzig, A.; Douspis, M.; Malavasi, N. First detection of stacked X-ray emission from cosmic web filaments. *Astropart. Phys.* **2020**, *643*, L2. [CrossRef]
4. Reiprich, T.H.; Veronica, A.; Pacaud, F.; Ramos-Ceja, M.E.; Ota, N.; Sanders, J.; Kara, M.; Erben, T.; Klein, M.; Erler, J.; et al. The Abell 3391/95 galaxy cluster system. A 15 Mpc intergalactic medium emission filament, a warm gas bridge, infalling matter clumps, and (re-) accelerated plasma discovered by combining SRG/eROSITA data with ASKAP/EMU and DECam data. *Astropart. Phys.* **2021**, *647*, A2. [CrossRef]
5. Walter, F.; Carilli, C.; Neeleman, M.; Decarli, R.; Popping, G.; Somerville, R.S.; Aravena, M.; Bertoldi, F.; Boogaard, L.; Cox, P.; et al. The Evolution of the Baryons Associated with Galaxies Averaged over Cosmic Time and Space. *Astrophys. J.* **2020**, *902*, 111. [CrossRef]
6. Nicastro, F.; Kaastra, J.; Krongold, Y.; Borgani, S.; Branchini, E.; Cen, R.; Dadina, M.; Danforth, C.W.; Elvis, M.; Fiore, F.; et al. Observations of the missing baryons in the warm-hot intergalactic medium. *Nature* **2018**, *558*, 406–409. [CrossRef] [PubMed]
7. Nath, B.B.; Silk, J. Heating of the intergalactic medium as a result of structure formation. *Mon. Not. R. Astron. Soc.* **2001**, *327*, L5–L9. [CrossRef]
8. Scannapieco, E.; Silk, J.; Bouwens, R. AGN Feedback Causes Downsizing. *Astrophys. J. Let.* **2005**, *635*, L13–L16. [CrossRef]
9. Cen, R.; Ostriker, J.P. Where Are the Baryons? II. Feedback Effects. *Astrophys. J.* **2006**, *650*, 560–572. [CrossRef]
10. Vacca, V.; Murgia, M.; Govoni, F.; Enßlin, T.; Oppermann, N.; Feretti, L.; Giovannini, G.; Loi, F. Magnetic Fields in Galaxy Clusters and in the Large-Scale Structure of the Universe. *Galaxies* **2018**, *6*, 142. [CrossRef]
11. Carretti, E.; O'Sullivan, S.P.; Vacca, V.; Vazza, F.; Gheller, C.; Vernstrom, T.; Bonafede, A. Magnetic field evolution in cosmic filaments with LOFAR data. *Mon. Not. R. Astron. Soc.* **2023**, *518*, 2273–2286. [CrossRef]
12. Kronberg, P.P. Extragalactic magnetic fields. *Rep. Prog. Phys.* **1994**, *57*, 325–382. [CrossRef]
13. Bertone, S.; Vogt, C.; Enßlin, T. Magnetic field seeding by galactic winds. *Mon. Not. R. Astron. Soc.* **2006**, *370*, 319–330. [CrossRef]
14. Vazza, F.; Brüggen, M.; Gheller, C.; Hackstein, S.; Wittor, D.; Hinz, P.M. Simulations of extragalactic magnetic fields and of their observables. *Class. Quantum Gravity* **2017**, *34*, 234001. [CrossRef]
15. Heesen, V.; O'Sullivan, S.P.; Brüggen, M.; Basu, A.; Beck, R.; Seta, A.; Carretti, E.; Krause, M.G.H.; Haverkorn, M.; Hutschenreuter, S.; et al. Detection of magnetic fields in the circumgalactic medium of nearby galaxies using Faraday rotation. *Astropart. Phys.* **2023**, *670*, L23. [CrossRef]
16. Akamatsu, H.; Fujita, Y.; Akahori, T.; Ishisaki, Y.; Hayashida, K.; Hoshino, A.; Mernier, F.; Yoshikawa, K.; Sato, K.; Kaastra, J.S. Properties of the cosmological filament between two clusters: A possible detection of a large-scale accretion shock by Suzaku. *Astropart. Phys.* **2017**, *606*, A1. [CrossRef]
17. Vernstrom, T.; West, J.; Vazza, F.; Wittor, D.; Riseley, C.J.; Heald, G. Polarized accretion shocks from the cosmic web. *Sci. Adv.* **2023**, *9*, eade7233. [CrossRef] [PubMed]
18. Thomas, T.; Pfrommer, C.; Pakmor, R. Cosmic-ray-driven galactic winds: Transport modes of cosmic rays and Alfvén-wave dark regions. *Mon. Not. R. Astron. Soc.* **2023**, *521*, 3023–3042. [CrossRef]
19. Ptuskin, V.; Rogovaya, S.; Zirakashvili, V. On ultra-high energy cosmic rays: Origin in AGN jets and transport in expanding universe. *Adv. Space Res.* **2013**, *51*, 315–321. [CrossRef]
20. Galárraga-Espinosa, D.; Cadiou, C.; Gouin, C.; White, S.D.M.; Springel, V.; Pakmor, R.; Hadzhiyska, B.; Bose, S.; Ferlito, F.; Hernquist, L.; et al. Evolution of cosmic filaments in the MTNG simulation. *arXiv* **2023**, arXiv:2309.08659.
21. Kampert, K.H.; Tinyakov, P. Cosmic rays from the ankle to the cutoff. *Comptes Rendus Phys.* **2014**, *15*, 318–328. [CrossRef]

22. Kampert, K.H. Ultra-high energy cosmic rays: Recent results and future plans of Auger. In *E*xotic Nuclei and Nuclear/Particle AstroPhysics (VI). Physics with Small Accelerators, Proceedings of the Carpathian Summer School of Physics 2016 (CSSP16), Sinaia, Romania, 26 June–9 July 2016; American Institute of Physics Conference Series; AIP Publishing: Melville, NY, USA, 2017; Volume 1852, p. 040001. [CrossRef]
23. Owen, E.R.; Han, Q.; Wu, K.; Yap, Y.X.J.; Surajbali, P. Ultra-High-energy Cosmic Rays from beyond the Greisen-Zatsepin-Kuz'min Horizon. *Astrophys. J.* **2021**, *922*, 32. [CrossRef]
24. Ziegler, J.F. Terrestrial cosmic ray intensities. *IBM J. Res. Dev.* **1998**, *42*, 117–140. [CrossRef]
25. Sato, T. Analytical Model for Estimating Terrestrial Cosmic Ray Fluxes Nearly Anytime and Anywhere in the World: Extension of PARMA/EXPACS. *PLoS ONE* **2015**, *10*, e0144679. [CrossRef] [PubMed]
26. Stone, E.C.; Cummings, A.C.; Heikkila, B.C.; Lal, N. Cosmic ray measurements from Voyager 2 as it crossed into interstellar space. *Nat. Astron.* **2019**, *3*, 1013–1018. [CrossRef]
27. Zhang, M.; Luo, X.; Pogorelov, N. Where is the cosmic-ray modulation boundary of the heliosphere? *Phys. Plasmas* **2015**, *22*, 091501. [CrossRef]
28. Rankin, J.S.; Stone, E.C.; Cummings, A.C.; McComas, D.J.; Lal, N.; Heikkila, B.C. Galactic Cosmic-Ray Anisotropies: Voyager 1 in the Local Interstellar Medium. *Astrophys. J.* **2019**, *873*, 46. [CrossRef]
29. Cummings, A.C.; Stone, E.C.; Heikkila, B.C.; Lal, N.; Webber, W.R.; Jóhannesson, G.; Moskalenko, I.V.; Orlando, E.; Porter, T.A. Galactic Cosmic Rays in the Local Interstellar Medium: Voyager 1 Observations and Model Results. *Astrophys. J.* **2016**, *831*, 18. [CrossRef] [PubMed]
30. Kissmann, R. PICARD: A novel code for the Galactic Cosmic Ray propagation problem. *Astropart. Phys.* **2014**, *55*, 37–50. [CrossRef]
31. Werner, M.; Kissmann, R.; Strong, A.W.; Reimer, O. Spiral arms as cosmic ray source distributions. *Astropart. Phys.* **2015**, *64*, 18–33. [CrossRef]
32. Globus, N.; Allard, D.; Parizot, E. A complete model of the cosmic ray spectrum and composition across the Galactic to extragalactic transition. *Phys. Rev. D* **2015**, *92*, 021302. [CrossRef]
33. Kempski, P.; Quataert, E. Reconciling cosmic ray transport theory with phenomenological models motivated by Milky-Way data. *Mon. Not. R. Astron. Soc.* **2022**, *514*, 657–674. [CrossRef]
34. Ambrosone, A.; Chianese, M.; Fiorillo, D.F.G.; Marinelli, A.; Miele, G. Observable signatures of cosmic rays transport in Starburst Galaxies on gamma-ray and neutrino observations. *Mon. Not. R. Astron. Soc.* **2022**, *515*, 5389–5399. [CrossRef]
35. Phan, V.H.M.; Recchia, S.; Mertsch, P.; Gabici, S. Stochasticity of cosmic rays from supernova remnants and the ionization rates in molecular clouds. *Phys. Rev. D* **2023**, *107*, 123006. [CrossRef]
36. Aharonian, F.; Peron, G.; Yang, R.; Casanova, S.; Zanin, R. Probing the sea of galactic cosmic rays with Fermi-LAT. *Phys. Rev. D* **2020**, *101*, 083018. [CrossRef]
37. Ajello, M.; Di Mauro, M.; Paliya, V.S.; Garrappa, S. The γ-Ray Emission of Star-forming Galaxies. *Astrophys. J.* **2020**, *894*, 88. [CrossRef]
38. Tibaldo, L.; Gaggero, D.; Martin, P. Gamma Rays as Probes of Cosmic-Ray Propagation and Interactions in Galaxies. *Universe* **2021**, *7*, 141. [CrossRef]
39. McCheyne, I.; Oliver, S.; Sargent, M.; Kondapally, R.; Smith, D.; Haskell, P.; Duncan, K.; Best, P.N.; Sabater, J.; Bonato, M.; et al. The LOFAR Two-metre Sky Survey Deep fields. The mass dependence of the far-infrared radio correlation at 150 MHz using deblended Herschel fluxes. *Astropart. Phys.* **2022**, *662*, A100. [CrossRef]
40. Yusef-Zadeh, F.; Wardle, M.; Arendt, R.; Hewitt, J.; Hu, Y.; Lazarian, A.; Kassim, N.E.; Hyman, S.; Heywood, I. Detection of large-scale synchrotron radiation from the molecular envelope of the Sgr B cloud complex at the Galactic centre. *Mon. Not. R. Astron. Soc.* **2024**, *527*, 1275–1282. [CrossRef]
41. Indriolo, N.; Bergin, E.A.; Falgarone, E.; Godard, B.; Zwaan, M.A.; Neufeld, D.A.; Wolfire, M.G. Constraints on the Cosmic-Ray Ionization Rate in the z $\sim$ 2.3 Lensed Galaxies SMM J2135-0102 and SDP 17b from Observations of OH^+ and H_2O^+. *Astrophys. J.* **2018**, *865*, 127. [CrossRef]
42. Okon, H.; Imai, M.; Tanaka, T.; Uchida, H.; Tsuru, T.G. Probing cosmic rays with Fe Kα line structures generated by multiple ionization process. *Pub. Astron. Soc. Jap.* **2020**, *72*, L7. [CrossRef]
43. Bialy, S. Cold clouds as cosmic-ray detectors. *Commun. Phys.* **2020**, *3*, 32. [CrossRef]
44. Pineda, J.E.; Sipilä, O.; Segura-Cox, D.M.; Valdivia-Mena, M.T.; Neri, R.; Kuffmeier, M.; Ivlev, A.V.; Offner, S.S.R.; Maureira, M.J.; Caselli, P.; et al. Probing the physics of star formation (ProPStar): I. First resolved maps of the electron fraction and cosmic-ray ionization rate in NGC 1333. *arXiv* **2024**, arXiv:2402.16202.
45. Kotera, K.; Olinto, A.V. The Astrophysics of Ultrahigh-Energy Cosmic Rays. *Annu. Rev. Astron. Astrophys.* **2011**, *49*, 119–153. [CrossRef]
46. Grenier, I.A.; Black, J.H.; Strong, A.W. The Nine Lives of Cosmic Rays in Galaxies. *Annu. Rev. Astron. Astrophys.* **2015**, *53*, 199–246. [CrossRef]
47. Ruszkowski, M.; Pfrommer, C. Cosmic ray feedback in galaxies and galaxy clusters. *Astron. Astrophys. Rev.* **2023**, *31*, 4. [CrossRef] [PubMed]
48. Owen, E.R.; Wu, K.; Inoue, Y.; Yang, H.Y.K.; Mitchell, A.M.W. Cosmic Ray Processes in Galactic Ecosystems. *Galaxies* **2023**, *11*, 86. [CrossRef]

49. Dermer, C.D.; Menon, G. *High Energy Radiation from Black Holes: Gamma Rays, Cosmic Rays, and Neutrinos*; Princeton University Press: Princeton, NJ, USA, 2009.
50. Bethe, H.; Heitler, W. On the Stopping of Fast Particles and on the Creation of Positive Electrons. *Proc. R. Soc. Lond. Ser. A* **1934**, *146*, 83–112. [CrossRef]
51. Blumenthal, G.R. Energy Loss of High-Energy Cosmic Rays in Pair-Producing Collisions with Ambient Photons. *Phys. Rev. D* **1970**, *1*, 1596–1602. [CrossRef]
52. Klein, S.R. e^+e^- Pair production from 10 GeV to 10 ZeV. *Radiat. Phys. Chem.* **2006**, *75*, 696–711. [CrossRef]
53. Hooper, D.; Plant, K. Leptonic Model for Neutrino Emission from Active Galactic Nuclei. *Phys. Rev. Lett.* **2023**, *131*, 231001. [CrossRef] [PubMed]
54. Almeida, S.P.; Rushbrooke, J.G.; Scharenguivel, J.H.; Behrens, M.; Blobel, V.; Borecka, I.; Dehne, H.C.; Dfaz, J.; Knies, G.; Schmitt, A.; et al. pp Interactions at 10 GeV/c. *Phys. Rev.* **1968**, *174*, 1638–1661. [CrossRef]
55. Skorodko, T.; Bashkanov, M.; Bogoslawsky, D.; Calen, H.; Cappellaro, F.; Clement, H.; Demiroers, L.; Doroshkevich, E.; Duniec, D.; Ekström, C.; et al. Excitation of the Roper resonance in single- and double-pion production in nucleon-nucleon collisions*. *Eur. Phys. J. A* **2008**, *35*, 317–319. [CrossRef]
56. Kafexhiu, E.; Aharonian, F.; Taylor, A.M.; Vila, G.S. Parametrization of gamma-ray production cross sections for p p interactions in a broad proton energy range from the kinematic threshold to PeV energies. *Phys. Rev. D* **2014**, *90*, 123014. [CrossRef]
57. Galliano, F. Multi-Wavelength Study of Nearby Dwarf Galaxies: Properties of Low-Metallicity Interstellar Media. Ph.D. Thesis, CEA Saclay, Service d'Astrophysique, Gif-sur-Yvette, France, 2004.
58. Schreiber, C.; Elbaz, D.; Pannella, M.; Ciesla, L.; Wang, T.; Franco, M. Dust temperature and mid-to-total infrared color distributions for star-forming galaxies at $0 < z < 4$. *Astropart. Phys.* **2018**, *609*, A30. [CrossRef]
59. Aragón-Calvo, M.A.; van de Weygaert, R.; Jones, B.J.T. Multiscale phenomenology of the cosmic web. *Mon. Not. R. Astron. Soc.* **2010**, *408*, 2163–2187. [CrossRef]
60. Cautun, M.; van de Weygaert, R.; Jones, B.J.T.; Frenk, C.S. Evolution of the cosmic web. *Mon. Not. R. Astron. Soc.* **2014**, *441*, 2923–2973. [CrossRef]
61. Zhu, W.; Zhang, F.; Feng, L.L. Profiles of Cosmic Filaments Since z = 4.0 in Cosmological Hydrodynamical Simulation. *Astrophys. J.* **2021**, *920*, 2. [CrossRef]
62. Gouin, C.; Gallo, S.; Aghanim, N. Gas distribution from clusters to filaments in IllustrisTNG. *Astropart. Phys.* **2022**, *664*, A198. [CrossRef]
63. Harikane, Y.; Ouchi, M.; Ono, Y.; Fujimoto, S.; Donevski, D.; Shibuya, T.; Faisst, A.L.; Goto, T.; Hatsukade, B.; Kashikawa, N.; et al. SILVERRUSH. VIII. Spectroscopic Identifications of Early Large-scale Structures with Protoclusters over 200 Mpc at $z \sim 6$-7: Strong Associations of Dusty Star-forming Galaxies. *Astrophys. J.* **2019**, *883*, 142. [CrossRef]
64. Di Mascolo, L.; Saro, A.; Mroczkowski, T.; Borgani, S.; Churazov, E.; Rasia, E.; Tozzi, P.; Dannerbauer, H.; Basu, K.; Carilli, C.L.; et al. Forming intracluster gas in a galaxy protocluster at a redshift of 2.16. *Nature* **2023**, *615*, 809–812. [CrossRef] [PubMed]
65. Wen, Z.L.; Han, J.L.; Liu, F.S. A Catalog of 132,684 Clusters of Galaxies Identified from Sloan Digital Sky Survey III. *Astrophys. J. Suppl.* **2012**, *199*, 34. [CrossRef]
66. VERITAS Collaboration.; Acciari, V.A.; Aliu, E.; Arlen, T.; Aune, T.; Bautista, M.; Beilicke, M.; Benbow, W.; Boltuch, D.; Bradbury, S.M.; et al. A connection between star formation activity and cosmic rays in the starburst galaxy M82. *Nature* **2009**, *462*, 770–772. [CrossRef]
67. Romero, G.E.; Müller, A.L.; Roth, M. Particle acceleration in the superwinds of starburst galaxies. *Astropart. Phys.* **2018**, *616*, A57. [CrossRef]
68. Lunardini, C.; Vance, G.S.; Emig, K.L.; Windhorst, R.A. Are starburst galaxies a common source of high energy neutrinos and cosmic rays? *J. Cosmol. Astropart. Phys.* **2019**, *2019*, 073. [CrossRef]
69. Hopkins, A.M.; Beacom, J.F. On the Normalization of the Cosmic Star Formation History. *Astrophys. J.* **2006**, *651*, 142–154. [CrossRef]
70. Förster Schreiber, N.M.; Wuyts, S. Star-Forming Galaxies at Cosmic Noon. *Annu. Rev. Astron. Astrophys.* **2020**, *58*, 661–725. [CrossRef]
71. Wolf, C.; Wisotzki, L.; Borch, A.; Dye, S.; Kleinheinrich, M.; Meisenheimer, K. The evolution of faint AGN between $z \simeq 1$ and $z \simeq 5$ from the COMBO-17 survey. *Astropart. Phys.* **2003**, *408*, 499–514. :20030990 [CrossRef]
72. Gray, W.J.; Scannapieco, E. Thermal and Chemical Evolution of Collapsing Filaments. *Astrophys. J.* **2013**, *768*, 174. [CrossRef]
73. Bharadwaj, S.; Bhavsar, S.P.; Sheth, J.V. The Size of the Longest Filaments in the Universe. *Astrophys. J.* **2004**, *606*, 25–31. [CrossRef]
74. Sarkar, P.; Pandey, B.; Sarkar, S. The maximum extent of the filaments and sheets in the cosmic web: An analysis of the SDSS DR17. *Mon. Not. R. Astron. Soc.* **2023**, *519*, 3227–3236. [CrossRef]
75. Pandey, B.; Kulkarni, G.; Bharadwaj, S.; Souradeep, T. The size of the longest filament in the luminous red galaxy distribution. *Mon. Not. R. Astron. Soc.* **2011**, *411*, 332–336. [CrossRef]
76. Wang, P.; Libeskind, N.I.; Tempel, E.; Kang, X.; Guo, Q. Possible observational evidence for cosmic filament spin. *Nat. Astron.* **2021**, *5*, 839–845. [CrossRef]
77. Greisen, K. End to the Cosmic-Ray Spectrum? *Phys. Rev. Lett.* **1966**, *16*, 748–750. [CrossRef]
78. Zatsepin, G.T.; Kuz'min, V.A. Upper Limit of the Spectrum of Cosmic Rays. *Sov. J. Exp. Theor. Phys. Lett.* **1966**, *4*, 78.

79. Owen, E.R.; Wu, K.; Jin, X.; Surajbali, P.; Kataoka, N. Starburst and post-starburst high-redshift protogalaxies. The feedback impact of high energy cosmic rays. *Astropart. Phys.* **2019**, *626*, A85. [CrossRef]
80. Planck Collaboration.; Aghanim, N.; Akrami, Y.; Ashdown, M.; Aumont, J.; Baccigalupi, C.; Ballardini, M.; Banday, A.J.; Barreiro, R.B.; Bartolo, N.; et al. Planck 2018 results. VI. Cosmological parameters. *Astropart. Phys.* **2020**, *641*, A6. [CrossRef]
81. Hillas, A.M. The Origin of Ultra-High-Energy Cosmic Rays. *Annu. Rev. Astron. Astrophys.* **1984**, *22*, 425–444. [CrossRef]
82. Hackstein, S.; Vazza, F.; Brüggen, M.; Sigl, G.; Dundovic, A. Propagation of ultrahigh energy cosmic rays in extragalactic magnetic fields: A view from cosmological simulations. *Mon. Not. R. Astron. Soc.* **2016**, *462*, 3660–3671. [CrossRef]
83. Pshirkov, M.S.; Tinyakov, P.G.; Urban, F.R. New Limits on Extragalactic Magnetic Fields from Rotation Measures. *Phys. Rev. Lett.* **2016**, *116*, 191302. [CrossRef]
84. Ackermann, M.; Ajello, M.; Baldini, L.; Ballet, J.; Barbiellini, G.; Bastieri, D.; Bellazzini, R.; Bissaldi, E.; Blandford, R.D.; Bloom, E.D.; et al. The Search for Spatial Extension in High-latitude Sources Detected by the Fermi Large Area Telescope. *Astrophys. J. Suppl.* **2018**, *237*, 32. [CrossRef]
85. Vovk, I. Search of the pair echo signatures in the high-energy light curve of GRB190114C. *Phys. Rev. D* **2023**, *107*, 043020. [CrossRef]
86. Durrer, R.; Neronov, A. Cosmological magnetic fields: Their generation, evolution and observation. *Astron. Astrophys. Rev.* **2013**, *21*, 62. [CrossRef]
87. Han, J.L. Observing Interstellar and Intergalactic Magnetic Fields. *Annu. Rev. Astron. Astrophys.* **2017**, *55*, 111–157. [CrossRef]
88. Xu, S.; Zhang, B. Probing the Intergalactic Turbulence with Fast Radio Bursts. *Astrophys. J. Let.* **2020**, *898*, L48. [CrossRef]
89. Bolton, J.S.; Gaikwad, P.; Haehnelt, M.G.; Kim, T.S.; Nasir, F.; Puchwein, E.; Viel, M.; Wakker, B.P. Limits on non-canonical heating and turbulence in the intergalactic medium from the low redshift Lyman α forest. *Mon. Not. R. Astron. Soc.* **2022**, *513*, 864–885. [CrossRef]
90. Carretti, E.; Vacca, V.; O'Sullivan, S.P.; Heald, G.H.; Horellou, C.; Röttgering, H.J.A.; Scaife, A.M.M.; Shimwell, T.W.; Shulevski, A.; Stuardi, C.; et al. Magnetic field strength in cosmic web filaments. *Mon. Not. R. Astron. Soc.* **2022**, *512*, 945–959. [CrossRef]
91. Xu, S.; Yan, H. Cosmic-Ray Parallel and Perpendicular Transport in Turbulent Magnetic Fields. *Astrophys. J.* **2013**, *779*, 140. [CrossRef]
92. Xu, W.; Fang, L.Z.; Wu, X.P. Virialization of Galaxy Clusters and Beyond. *Astrophys. J.* **2000**, *532*, 728–739. [CrossRef]
93. Tully, R.B.; Courtois, H.; Hoffman, Y.; Pomarède, D. The Laniakea supercluster of galaxies. *Nature* **2014**, *513*, 71–73. [CrossRef]
94. Keppens, R.; Goedbloed, J.P. Stellar Winds, Dead Zones, and Coronal Mass Ejections. *Astrophys. J.* **2000**, *530*, 1036–1048. [CrossRef]
95. Wiegelmann, T.; Petrie, G.J.D.; Riley, P. Coronal Magnetic Field Models. *Space Sci, Rev.* **2017**, *210*, 249–274. [CrossRef]
96. Vazza, F.; Locatelli, N.; Rajpurohit, K.; Banfi, S.; Domínguez-Fernández, P.; Wittor, D.; Angelinelli, M.; Inchingolo, G.; Brienza, M.; Hackstein, S.; et al. Magnetogenesis and the Cosmic Web: A Joint Challenge for Radio Observations and Numerical Simulations. *Galaxies* **2021**, *9*, 109. [CrossRef]
97. Govoni, F.; Feretti, L. Magnetic Fields in Clusters of Galaxies. *Int. J. Mod. Phys. D* **2004**, *13*, 1549–1594. [CrossRef]
98. Beck, R. Magnetic fields in spiral galaxies. *Astron. Astrophys. Rev.* **2015**, *24*, 4. [CrossRef]
99. Peretti, E.; Blasi, P.; Aharonian, F.; Morlino, G. Cosmic ray transport and radiative processes in nuclei of starburst galaxies. *Mon. Not. R. Astron. Soc.* **2019**, *487*, 168–180. [CrossRef]
100. Beck, A.M.; Hanasz, M.; Lesch, H.; Remus, R.S.; Stasyszyn, F.A. On the magnetic fields in voids. *Mon. Not. R. Astron. Soc.* **2013**, *429*, L60–L64. [CrossRef]
101. Samui, S.; Subramanian, K.; Srianand, R. Efficient cold outflows driven by cosmic rays in high-redshift galaxies and their global effects on the IGM. *Mon. Not. R. Astron. Soc.* **2018**, *476*, 1680–1695. [CrossRef]
102. Bagchi, J.; Sankhyayan, S.; Sarkar, P.; Raychaudhury, S.; Jacob, J.; Dabhade, P. Saraswati: An Extremely Massive ∼200 Megaparsec Scale Supercluster. *Astrophys. J.* **2017**, *844*, 25. [CrossRef]
103. Han, J.L.; Manchester, R.N.; Lyne, A.G.; Qiao, G.J.; van Straten, W. Pulsar Rotation Measures and the Large-Scale Structure of the Galactic Magnetic Field. *Astrophys. J.* **2006**, *642*, 868–881. [CrossRef]
104. Rix, H.W.; Bovy, J. The Milky Way's stellar disk. Mapping and modeling the Galactic disk. *Astron. Astrophys. Rev.* **2013**, *21*, 61. [CrossRef]
105. Hayden, M.R.; Recio-Blanco, A.; de Laverny, P.; Mikolaitis, S.; Worley, C.C. The AMBRE project: The thick thin disk and thin thick disk of the Milky Way. *Astropart. Phys.* **2017**, *608*, L1. [CrossRef]
106. Vietri, M. The Acceleration of Ultra–High-Energy Cosmic Rays in Gamma-Ray Bursts. *Astrophys. J.* **1995**, *453*, 883. [CrossRef]
107. Pierre Auger Collaboration.; Abraham, J.; Abreu, P.; Aglietta, M.; Aguirre, C.; Allard, D.; Allekotte, I.; Allen, J.; Allison, P.; Alvarez-Muñiz, J.; et al. Correlation of the highest-energy cosmic rays with the positions of nearby active galactic nuclei. *Astropart. Phys.* **2008**, *29*, 188–204. [CrossRef]
108. Anchordoqui, L.A.; Torres, D.F. Exploring the superwind mechanism for generating ultrahigh-energy cosmic rays using large-scale modeling of starbursts. *Phys. Rev. D* **2020**, *102*, 023034. [CrossRef]
109. Mora, S.C.; Krause, M. Magnetic field structure and halo in NGC 4631. *Astropart. Phys.* **2013**, *560*, A42. [CrossRef]
110. Krause, M. Magnetic Fields and Star Formation in Spiral Galaxies. *Rev. Mex. Astron. Astrofis. Conf. Ser.* **2009**, *36*, 25–29.

111. Pattle, K.; Gear, W.; Redman, M.; Smith, M.W.L.; Greaves, J. Submillimetre observations of the two-component magnetic field in M82. *Mon. Not. R. Astron. Soc.* **2021**, *505*, 684–688. [CrossRef]
112. Karachentseva, V.E.; Karachentsev, I.D.; Kaisina, E.I.; Kaisin, S.S. The M 101 galaxy group as a node in a nearby cosmic filament. *Astropart. Phys.* **2023**, *678*, A16. [CrossRef]
113. Kotera, K.; Lemoine, M. Optical depth of the Universe to ultrahigh energy cosmic ray scattering in the magnetized large scale structure. *Phys. Rev. D* **2008**, *77*, 123003. [CrossRef]
114. Owen, E.R.; Han, Q.; Wu, K. Effects of large-scale magnetic fields on the observed composition of ultrahigh-energy cosmic rays. *Phys. Rev. D* **2023**, *107*, 103027. [CrossRef]
115. Tempel, E.; Stoica, R.S.; Martínez, V.J.; Liivamägi, L.J.; Castellan, G.; Saar, E. Detecting filamentary pattern in the cosmic web: A catalogue of filaments for the SDSS. *Mon. Not. R. Astron. Soc.* **2014**, *438*, 3465–3482. [CrossRef]
116. Bustard, C.; Zweibel, E.G. Cosmic-Ray Transport, Energy Loss, and Influence in the Multiphase Interstellar Medium. *Astrophys. J.* **2021**, *913*, 106. [CrossRef]
117. Butsky, I.S.; Hopkins, P.F.; Kempski, P.; Ponnada, S.B.; Quataert, E.; Squire, J. Galactic cosmic-ray scattering due to intermittent structures. *Mon. Not. R. Astron. Soc.* **2024**, *528*, 4245–4254. [CrossRef]
118. Tharakkal, D.; Snodin, A.P.; Sarson, G.R.; Shukurov, A. Cosmic rays and random magnetic traps. *Physical Review E* **2023**, *107*, 065206. [CrossRef] [PubMed]
119. Le Vot, F.; Abad, E.; Yuste, S.B. Continuous-time random-walk model for anomalous diffusion in expanding media. *Phys. Rev. E* **2017**, *96*, 032117. [CrossRef] [PubMed]
120. Libeskind, N.I.; van de Weygaert, R.; Cautun, M.; Falck, B.; Tempel, E.; Abel, T.; Alpaslan, M.; Aragón-Calvo, M.A.; Forero-Romero, J.E.; Gonzalez, R.; et al. Tracing the cosmic web. *Mon. Not. R. Astron. Soc.* **2018**, *473*, 1195–1217. [CrossRef]
121. Dubkov, A.A.; Spagnolo, B.; Uchaikin, V.V. LÉVY Flight Superdiffusion: AN Introduction. *Int. J. Bifurc. Chaos* **2008**, *18*, 2649. [CrossRef]
122. Humphries, N.E.; Sims, D.W. Optimal foraging strategies: Lévy walks balance searching and patch exploitation under a very broad range of conditions. *J. Theor. Biol.* **2014**, *358*, 179–193. [CrossRef]
123. Dubkov, A.A.; Kharcheva, A.A. Features of barrier crossing event for Lévy flights. *EPL (Europhys. Lett.)* **2016**, *113*, 30009. [CrossRef]
124. Garbaczewski, P. Killing (absorption) versus survival in random motion. *Physical Review E* **2017**, *96*, 032104. [CrossRef] [PubMed]
125. Zhang, C.; Xu, S. Numerical Testing of Mirror Diffusion of Cosmic Rays. *Astrophys. J. Let.* **2023**, *959*, L8. [CrossRef]
126. Aharonian, F.A. Proton-synchrotron radiation of large-scale jets in active galactic nuclei. *Mon. Not. R. Astron. Soc.* **2002**, *332*, 215–230. [CrossRef]
127. Gaisser, T.K.; Stanev, T.; Tilav, S. Cosmic ray energy spectrum from measurements of air showers. *Front. Phys.* **2013**, *8*, 748–758. [CrossRef]
128. Alves Batista, R.; Biteau, J.; Bustamante, M.; Dolag, K.; Engel, R.; Fang, K.; Kampert, K.H.; Kostunin, D.; Mostafa, M.; Murase, K.; et al. Open Questions in Cosmic-Ray Research at Ultrahigh Energies. *Front. Astron. Space Sci.* **2019**, *6*, 23. [CrossRef]
129. Aloisio, R.; Berezinsky, V.; Gazizov, A. Transition from galactic to extragalactic cosmic rays. *Astropart. Phys.* **2012**, *39*, 129–143. [CrossRef]
130. Dolag, K.; Grasso, D.; Springel, V.; Tkachev, I. Constrained simulations of the magnetic field in the local Universe and the propagation of ultrahigh energy cosmic rays. *J. Cosmol. Astropart. Phys.* **2005**, *2005*, 009. [CrossRef]
131. Madau, P.; Dickinson, M. Cosmic Star-Formation History. *Annu. Rev. Astron. Astrophys.* **2014**, *52*, 415–486. [CrossRef]
132. Galárraga-Espinosa, D.; Langer, M.; Aghanim, N. Relative distribution of dark matter, gas, and stars around cosmic filaments in the IllustrisTNG simulation. *Astropart. Phys.* **2022**, *661*, A115. [CrossRef]
133. Ricciardelli, E.; Quilis, V.; Planelles, S. The structure of cosmic voids in a ΛCDM Universe. *Mon. Not. R. Astron. Soc.* **2013**, *434*, 1192–1204. [CrossRef]
134. Abdalla, H.; Böttcher, M. EBL Inhomogeneity and Hard-Spectrum Gamma-Ray Sources. *Astrophys. J.* **2017**, *835*, 237. [CrossRef]
135. Adermann, E.; Elahi, P.J.; Lewis, G.F.; Power, C. Cosmic voids in evolving dark sector cosmologies: The high-redshift universe. *Mon. Not. R. Astron. Soc.* **2018**, *479*, 4861–4877. [CrossRef]
136. Rowan-Robinson, M. Hyperluminous infrared galaxies. *Mon. Not. R. Astron. Soc.* **2000**, *316*, 885–900. [CrossRef]
137. Moser, E.; Battaglia, N.; Nagai, D.; Lau, E.; Machado Poletti Valle, L.F.; Villaescusa-Navarro, F.; Amodeo, S.; Anglés-Alcázar, D.; Bryan, G.L.; Dave, R.; et al. The Circumgalactic Medium from the CAMELS Simulations: Forecasting Constraints on Feedback Processes from Future Sunyaev-Zeldovich Observations. *Astrophys. J.* **2022**, *933*, 133. [CrossRef]
138. Laganá, T.F.; Martinet, N.; Durret, F.; Lima Neto, G.B.; Maughan, B.; Zhang, Y.Y. A comprehensive picture of baryons in groups and clusters of galaxies. *Astropart. Phys.* **2013**, *555*, A66. [CrossRef]
139. Oppenheimer, B.D.; Babul, A.; Bahé, Y.; Butsky, I.S.; McCarthy, I.G. Simulating Groups and the IntraGroup Medium: The Surprisingly Complex and Rich Middle Ground between Clusters and Galaxies. *Universe* **2021**, *7*, 209. [CrossRef]
140. Bitsakis, T.; Charmandaris, V.; da Cunha, E.; Díaz-Santos, T.; Le Floc'h, E.; Magdis, G. A mid-IR study of Hickson compact groups. II. Multiwavelength analysis of the complete GALEX-Spitzer sample. *Astropart. Phys.* **2011**, *533*, A142. [CrossRef]

141. Cole, S.; Lacey, C. The structure of dark matter haloes in hierarchical clustering models. *Mon. Not. R. Astron. Soc.* **1996**, *281*, 716. [CrossRef]
142. Longobardi, A.; Boselli, A.; Boissier, S.; Bianchi, S.; Andreani, P.; Sarpa, E.; Nanni, A.; Miville-Deschênes, M. The GALEX Ultraviolet Virgo Cluster Survey (GUViCS). VIII. Diffuse dust in the Virgo intra-cluster space. *Astropart. Phys.* **2020**, *633*, L7. [CrossRef]